

1 **Susceptibility of Marine Warm Clouds to Aerosols in**  
2 **Different Monsoon Periods over the South China Sea**

3 Yan Liu<sup>1</sup>, Hailing Jia<sup>2</sup>, Yong Han<sup>1\*</sup>

4 <sup>1</sup>Advanced Science & Technology of Space and Atmospheric Physics Group (ASAG), School of  
5 Atmospheric Sciences, Sun Yat-sen University, 519082 Zhuhai, China

6 <sup>2</sup>SRON Space Research Organisation Netherlands, Leiden, The Netherlands

7 \* *Correspondence to:* Yong Han (hany66@mail.sysu.edu.cn)

8

9 **Abstract.**

10 Understanding the susceptibility of warm clouds to aerosol loading, quantified by the aerosol–cloud  
11 interactions (ACI) index, is essential for assessing ACI and their climate impacts. Previous studies have  
12 demonstrated that this susceptibility is strongly modulated by environmental conditions. The South  
13 China Sea (SCS), influenced alternately by the southwest and northeast monsoons, provides a unique  
14 natural laboratory for examining ACI under contrasting thermodynamic and moisture conditions. Using  
15 long-term satellite observations and reanalysis data, we investigate ACI in non-raining warm liquid  
16 clouds over the SCS across three monsoon phases: the southwest monsoon wet period (SWMW),  
17 northeast monsoon wet period (NEMW), and northeast monsoon dry period (NEMD). The robust  
18 Twomey effect is observed across all periods. Shallow stratocumulus clouds show no significant  
19 differences in ACI across periods, whereas deeper cumulus clouds exhibit the strongest ACI during  
20 NEMD, with no clear separation between SWMW and NEMW. The enhanced ACI during NEMD is  
21 consistent with the relatively dry and stable lower-tropospheric environment (LTS), where stable  
22 conditions may enhance ACI through aerosol accumulation, while moist environments are likely to  
23 weaken it via enhanced condensational and coalescence growth. However, these differences likely reflect  
24 co-varying environmental conditions across monsoon periods rather than a single dominant controlling  
25 factor. Limitations of AI as a marine cloud condensation nuclei (CCN) proxy and satellite retrieval biases  
26 may affect these conclusions. These findings suggest that, within a monsoon-organized framework, the  
27 interplay among aerosols, humidity, and stability is associated with marine warm-cloud microphysics,  
28 providing observational constraints for climate model representation of ACI.

- 删除了: a progressive increase from
- 删除了: to
- 删除了: and NEMD, corresponding to transitions from moist convective to...
- 删除了: environments. This variability is likely governed by water-vapor availability and
- 删除了: stability
- 删除了: reveal the dominant roles of thermodynamic stability and moisture in regulating ACI over the SCS. The
- 删除了: governs
- 删除了: in tropical monsoon environments
- 删除了: improving the
- 删除了: in climate models

30 **1 Introduction**

31 Aerosol–cloud interactions (ACI) play a crucial role in regulating Earth’s radiative balance and  
32 hydrological cycle by altering cloud microphysical and macrophysical properties (Bellouin et al., 2020;  
33 Jia et al., 2021; Rosenfeld et al., 2019; Stier et al., 2024; Wang et al., 2024c; Zhao et al., 2024). Numerous  
34 studies have demonstrated that ACI are strongly modulated by environmental conditions, such as lower-  
35 tropospheric stability (Chen et al., 2014; Wang et al., 2014), relative humidity (Douglas and L’Ecuyer,

49 2019), precipitable water vapor (Qiu et al., 2017; Yuan et al., 2008; Zheng et al., 2022), vertical velocity  
50 (Jia et al., 2022; Su et al., 2010), wind shear (Fan et al., 2009; Kim et al., 2003) , and the vertical overlap  
51 between aerosol and cloud layers (Costantino and Bréon, 2013). However, over the South China Sea  
52 (SCS), a region strongly influenced by pronounced monsoon circulation, the observational evidence of  
53 how ACI respond to variations in thermodynamic and moisture conditions remains limited.

54 The SCS, one of the world’s largest marginal seas, provides a unique natural laboratory for investigating  
55 ACI under the alternating influence of two opposing monsoon systems. The SCS experiences a  
56 pronounced seasonal reversal of wind regimes, characterized by a warm, moist southwest monsoon  
57 during boreal summer and a cool, dry northeast monsoon during boreal winter (Wang et al., 2009).  
58 During the southwest monsoon period, the marine boundary layer over the northern SCS becomes  
59 unstable, with enhanced air–sea temperature differences and surface turbulent heat fluxes that intensify  
60 vertical mixing and deepen the boundary layer while reducing wind shear (Peng et al., 2016). Rainfall  
61 during this period is primarily governed by warm-cloud microphysical processes and vapor convergence-  
62 driven condensation (Wang et al., 2007). In contrast, during the northeast monsoon period, cold surges  
63 associated with the East Asian winter monsoon substantially modify the SCS boundary-layer structure  
64 by enhancing surface turbulent fluxes, deepening the mixed layer, and strengthening the inversion that  
65 promotes extensive low-cloud development (Wang et al., 2024a). The SCS is also a region that is  
66 simultaneously affected by various types of aerosols from industrial emissions, shipping activities, and  
67 biomass burning. It has been shown that those aerosols substantially modify the microphysical structure  
68 of marine boundary layer clouds over the SCS by increasing small droplet concentrations and suppressing  
69 midsize droplets near cloud base (Miller et al., 2023). Recent shipborne observations further reveal that  
70 aerosol sources over the SCS exhibit distinct seasonal contrasts, being dominated by continental outflow  
71 from mainland Southeast Asia during the southwest monsoon and by pollution plumes transported from  
72 continental China during the northeast monsoon (Ou et al., 2025). Yet, how these contrasting aerosol and  
73 meteorological regimes modulate ACI, particularly for warm non-raining clouds, remains poorly  
74 quantified.

75 Quantifying ACI is essential for constraining their climatic impacts. According to the Sixth Assessment  
76 Report of the Intergovernmental Panel on Climate Change (Douville et al., 2023) , the effective radiative

77 forcing associated with ACI ( $ERF_{aci}$ ) is estimated to be  $-0.84 \text{ W m}^{-2}$  globally, with a wide 5–95%  
78 confidence range from  $-1.45 \text{ W m}^{-2}$  to  $-0.25 \text{ W m}^{-2}$ , dominating the overall uncertainty in total aerosol  
79 effective radiative forcing, which ranges between  $-1.7$  and  $-0.4 \text{ W m}^{-2}$ .  $ERF_{aci}$  may be further  
80 decomposed into two components: the instantaneous radiative forcing due to ACI, also known as the  
81 Twomey effect ( $RF_{aci}$ , Twomey, 1977, 1974), and rapid adjustments (Ackerman et al., 2004; Albrecht,  
82 1989; Bellouin et al., 2020). To quantify the cloud response to aerosol perturbations, Feingold et al.  
83 (2001) proposed the ACI index ( $ACI_r$  and  $ACI_{Nd}$ ), which has since become a widely used metric for  
84 evaluating the strength of the Twomey effect in both satellite and in-situ studies, defined as:

$$85 \quad ACI_r = -d \ln r / d \ln \alpha \quad (1)$$

$$86 \quad ACI_{Nd} = d \ln N_d / d \ln \alpha \quad (2)$$

87 where  $r$  and  $N_d$  denote the cloud effective radius and droplet number concentration, respectively, and  $\alpha$   
88 is an aerosol proxy (e.g., AOD, AI, or NCCN). In this study, AI is employed as the aerosol proxy in the  
89 calculation of ACI.  $ACI_{Nd}$  is more recently also referred to as the  $N_d$  susceptibility to aerosols (Ma et al.,  
90 2018a, b).

91 Although many studies have examined the environmental modulation of ACI over both oceanic and  
92 continental regions (Fan et al., 2016; Jia et al., 2019, 2022; Jia and Quaas, 2023; Seinfeld et al., 2016;  
93 Sorooshian et al., 2019; Wall et al., 2022; Wang et al., 2024d), such processes remain poorly constrained  
94 over the SCS. The pronounced seasonal reversal of monsoon circulation in this region creates highly  
95 contrasting thermodynamic and moisture conditions, along with differing aerosol regimes, which  
96 together exert distinct influences on cloud microphysics and modulate the ACI processes. Therefore, this  
97 study aims to provide a comprehensive assessment of ACI in non-raining warm clouds over the SCS  
98 under different monsoon regimes. Long-term multi-satellite and reanalysis datasets from July 2002 to  
99 February ~~2020~~ are integrated to characterize variations in aerosol, cloud, and environmental properties  
100 across the southwest monsoon wet (SWMW), northeast monsoon wet (NEMW), and northeast monsoon  
101 dry (NEMD) phases, and to quantitatively evaluate the corresponding ACI responses. Particular attention  
102 is given to understanding how variations in water vapor availability and lower-tropospheric stability  
103 (LTS) influence the sensitivity of cloud microphysical responses to aerosol perturbations.

删除了: 2023

105 The paper is organized as follows. Section 2 describes the datasets and method used in this study. The  
 106 main findings and related discussions are presented in Section 3. Section 4 summarizes the key findings  
 107 and conclusions.

108 **2 Data and Methods**

109 This study employs long-term, multi-source datasets to investigate ACI over the SCS. The cloud  
 110 properties are derived from the Clouds and the Earth’s Radiant Energy System (CERES)–Moderate  
 111 Resolution Imaging Spectroradiometer (MODIS) Edition 4 Level-3 product (SSF1deg, Aqua, daytime).  
 112 Cloud droplet number concentration (Nd) data are obtained from a community-standard gridded dataset  
 113 provided by Gryspeerdt et al. (2022). Aerosol optical properties is obtained from the Modern-Era  
 114 Retrospective analysis for Research and Applications, Version 2 (MERRA-2). Meteorological fields are  
 115 taken from the European Centre for Medium-Range Weather Forecasts (ECMWF) fifth-generation  
 116 reanalysis (ERA5). Precipitation data are provided by the Integrated Multi-satellite Retrievals for GPM  
 117 (IMERG) Version 7 Final Run, and sea surface temperature (SST) data are obtained from the National  
 118 Oceanic and Atmospheric Administration (NOAA) Optimum Interpolation (OI) SST, version 2. The  
 119 definitions of the monsoon regimes and the analyses of large-scale circulation, aerosol, and cloud  
 120 properties are conducted at their native spatial resolutions. For aerosol–cloud collocation, AOD, AI, and  
 121 ERA5 meteorological fields used in the calculation of ACI and environmental stratification are regridded  
 122 to a common  $1^\circ \times 1^\circ$  grid using bilinear interpolation with the Climate Data Operators (CDO, remapbil).

123 **Table 1: Overview of datasets used in this study.**

Parameter	Data Source	Spatial Resolution	Temporal Resolution	Data Range
Cloud Effective Radius	CERES–MODIS	$1^\circ \times 1^\circ$	daily	Jul 2002 –
Cloud Optical Thickness	V04 SSF1deg			Feb 2020
Cloud-top Temperature	(Aqua, daytime)			
Cloud-top Pressure				
Liquid Cloud Area Fraction				
Liquid Water Path				
Cloud <del>Droplet Number Concentration</del>	Gryspeerdt et al. (2022)	$1^\circ \times 1^\circ$	daily	Jul 2002 – Feb 2020
Total <del>Aerosol Extinction</del> (550 nm)	AOT MERRA-2	$0.5^\circ \times 0.625^\circ$	daily	Jul 2002 – Feb 2020

删除了: droplet number concentration

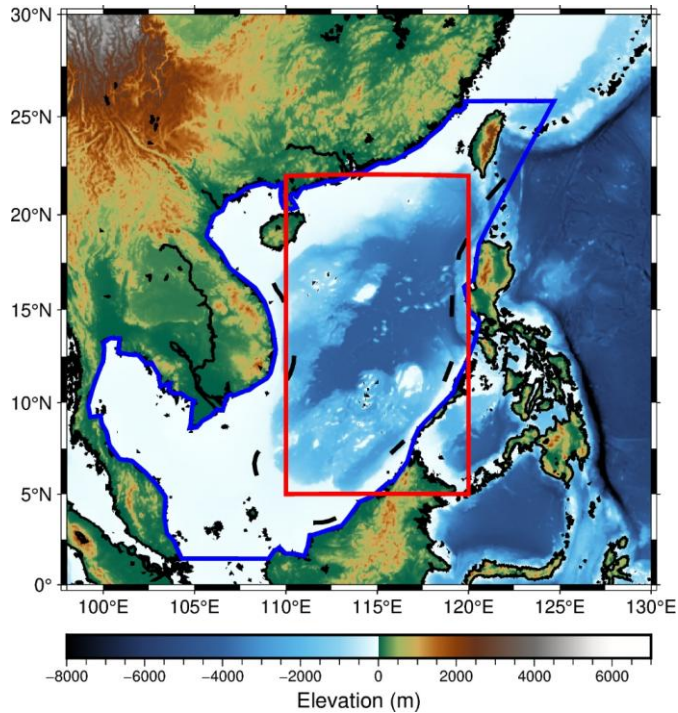
删除了: aerosol extinction

Total	<a href="#">Aerosol</a>	Ångström				
<a href="#">Parameter</a> (470–870 nm)						
Specific Humidity	ERA5		0.25°	×	daily	Jul 2002 –
<a href="#">Temperature</a>			0.25°			Feb 2020
<a href="#">Relative Humidity</a>						
<a href="#">Horizontal Wind Components</a>						
<a href="#">Mean Sea Level Pressure</a>						
▼ Precipitation	IMERG	V07	0.1° × 0.1°		30 min	Jul 2002 –
	Final					Feb 2020
Sea Surface Temperature	NOAA OI	SST	1° × 1°		monthly	Jul 2002 –
	V2					Feb 2020

- 删除了: aerosol
- 删除了: parameter
- 拆分的单元格
- 拆分的单元格
- 拆分的单元格
- 拆分的单元格
- 删除了: Temperature

126 **2.1 Study Area**

127 SCS is one of the world’s largest marginal seas, characterized by complex air–sea interactions and a  
 128 pronounced seasonal reversal of wind systems (Wang et al., 2009). This region is strongly influenced by  
 129 the Asian monsoon circulation, exhibiting distinct southwest and northeast monsoon regimes that  
 130 profoundly modulate its thermodynamic and dynamic environments (Zheng et al., 2025). These  
 131 alternating monsoon circulations govern the regional aerosol loading (Ou et al., 2025), boundary-layer  
 132 structure (Chen et al., 2025; Peng et al., 2016; Wang et al., 2024a), and cloud microphysical processes  
 133 (Miller et al., 2023; Wang et al., 2024b), making the SCS an ideal natural laboratory for investigating  
 134 ACI under contrasting meteorological conditions. In this study, the analysis domain (blue polygon in  
 135 Fig. 1) encompasses the entire SCS, including both coastal and open-ocean areas, to capture the spatial  
 136 variability of aerosol, cloud, and environmental parameters. The red box in Fig. 1 delineates the  
 137 subregion (3°–22° N, 110°–120° E) used for defining the monsoon regimes following Wang et al. (2004).



141

142 **Figure 1: Study region and monsoon classification over the South China Sea. The blue polygon indicates the**  
 143 **study domain, while the red box marks the region used for defining the monsoon regimes.**

144 **2.2 Cloud Remote Sensing Products**

145 Cloud retrievals used in this study are derived from the Moderate Resolution Imaging Spectroradiometer  
 146 (MODIS) aboard the Aqua satellite, which has an equatorial crossing time of approximately 1:30 p.m.  
 147 local time. The MODIS cloud products analysed are obtained from the Clouds and the Earth's Radiant  
 148 Energy System (CERES) MODIS (CERES–MODIS hereafter) Edition 4 (Minnis et al., 2011a, 2021)  
 149 Single Scanner Footprint (SSF) daily products (Level 3,  $1^\circ \times 1^\circ$  grid resolution), which provide  
 150 physically consistent cloud and radiative properties based on synergistic MODIS and CERES  
 151 observations. The CERES–MODIS cloud retrievals have been extensively validated (Minnis et al.,  
 152 2011b; Yost et al., 2021) and have been widely employed in studies of ACI (Jia et al., 2021; Painemal,  
 153 2018). CERES–MODIS Edition 4 SSF cloud parameters utilized here include cloud optical depth ( $\tau$ ),  
 154 cloud effective radius (CER), cloud-top temperature (CTT), cloud-top pressure (CTP), liquid cloud area

155 fraction (LCAF), and liquid water path (LWP). CER is retrieved from the 3.7- $\mu\text{m}$  channel, which is less  
156 affected by retrieval biases than its 2.1- and 1.6- $\mu\text{m}$  counterparts (Grosvenor et al., 2018).  
157  $N_d$  used in this study is obtained from the community-standard gridded dataset of Gryspeerdt et al.  
158 (2022), which provides  $1^\circ \times 1^\circ$  Level-3  $N_d$  products derived from pixel-level MODIS Collection 6.1  
159 retrievals. In this dataset,  $N_d$  is first estimated at the native MODIS pixel scale using retrieved cloud  
160 optical thickness and cloud effective radius, and then aggregated to a common grid using established  
161 sampling strategies to ensure robustness and consistency. The  $N_d$  retrievals are based on the adiabatic  
162 cloud assumption and are subject to strict quality control procedures, including screening for optically  
163 thin clouds, large solar zenith angle and viewing zenith angle conditions, sub-pixel heterogeneity, and  
164 potential retrieval contamination. Only single-layer liquid cloud scenes are retained. This dataset has  
165 been evaluated against observations and is widely used in aerosol–cloud interaction studies (e.g., Jia et  
166 al., 2024; Wall et al., 2023). In this study, we use the  $N_{d\_G18\_37}$  product from this community-standard  
167 dataset.

### 168 **2.3 Aerosol Optical Properties**

169 Aerosol properties used in this study are obtained from the Modern-Era Retrospective Analysis for  
170 Research and Applications, Version 2 (MERRA-2, Gelaro et al., 2017), which assimilates a wide range  
171 of satellite observations to provide a physically consistent representation of global aerosol distributions.  
172 The MERRA-2 aerosol dataset used here includes the total aerosol extinction (AOD, 550 nm) and the  
173 total aerosol Ångström parameter (AE, 470-870 nm), with a spatial resolution of  $0.5^\circ \times 0.625^\circ$  and a  
174 temporal resolution of 1 hour. To ensure spatiotemporal consistency with the CERES–MODIS cloud  
175 products, the MERRA-2 aerosol fields at 14:00 local solar time (LST), closest to the Aqua overpass  
176 ( $\sim 13:30$  LST), were regridded to a  $1^\circ \times 1^\circ$  grid. AOD represents the column-integrated aerosol extinction,  
177 whereas AE characterizes the wavelength dependence of AOD and is commonly used as an indicator of  
178 aerosol particle size. A higher AE generally indicates dominance of fine-mode aerosols, while a lower  
179 AE suggests coarse-mode particles. The aerosol index (AI) is defined as the product of AOD and AE:

$$180 \quad \text{AI} = \text{AOD} \times \text{AE} \quad (3)$$

181 AI, in comparison to AOD, is considered a better parameter for representing aerosols in ACI studies,  
182 because it incorporates information on aerosol particle size, which is critical for cloud droplet activation

183 and microphysical properties (Ma et al., 2018b; Nakajima et al., 2001). Therefore, AI is employed in this  
184 study as the aerosol proxy in the calculation of ACI.

#### 185 **2.4 Atmospheric Parameters of Weather Fields**

186 Atmospheric fields were obtained from the fifth-generation ECMWF reanalysis (ERA5, Hersbach et al.,  
187 2020). ERA5 assimilates a comprehensive suite of ground-based and satellite observations through a  
188 state-of-the-art four-dimensional variational data assimilation system, offering physically consistent and  
189 dynamically balanced representations of the atmosphere. The dataset used here includes three-  
190 dimensional fields of specific humidity and horizontal wind components (U and V) at all standard  
191 pressure levels, temperature at 1000 and 700 hPa, and mean sea level pressure. The daily mean specific  
192 humidity and wind speed at 850 hPa were used to distinguish the three periods over the SCS (Wang et  
193 al., 2004). Wind and humidity fields at all pressure levels were analysed to characterize the large-scale  
194 atmospheric circulation and vertical moisture structure during these periods. The 1000 hPa specific  
195 humidity was employed as a proxy for the ambient water vapor available to warm clouds (Dadashazar et  
196 al., 2020). Temperatures at 1000 and 700 hPa were used to compute the LTS, which quantifies the  
197 thermodynamic stability of the lower atmosphere (Klein and Hartmann, 1993), as follows:

198

$$199 \quad \begin{aligned} LTS &= \theta_{700\text{hPa}} - \theta_{1000\text{hPa}} \\ \theta &= T \left( \frac{P_{00}}{P} \right)^{\frac{R}{C_p}} \end{aligned} \quad (4)$$

200 where  $\theta_{700}$  and  $\theta_{1000}$  denote the potential temperatures at 700 and 1000 hPa, respectively,  $P_{00}$  is the  
201 standard reference pressure (typically 1000 hPa),  $P$  is the pressure at a given level,  $R$  is the gas constant  
202 for dry air, and  $C_p$  is the specific heat capacity of dry air at constant pressure. To ensure spatiotemporal  
203 consistency with the aerosol and cloud parameters, both the 1000 hPa specific humidity and LTS at 14:00  
204 LST were regridded to a  $1^\circ \times 1^\circ$  grid. Sea surface temperature (SST) was obtained from the National  
205 Oceanic and Atmospheric Administration (NOAA) Optimum Interpolation SST, version 2 (OI SST v2,  
206 Reynolds et al., 2002), which incorporates both in-situ and satellite observations and provides monthly  
207 fields at  $1^\circ \times 1^\circ$  resolution.

## 208 **2.5 Precipitation Data**

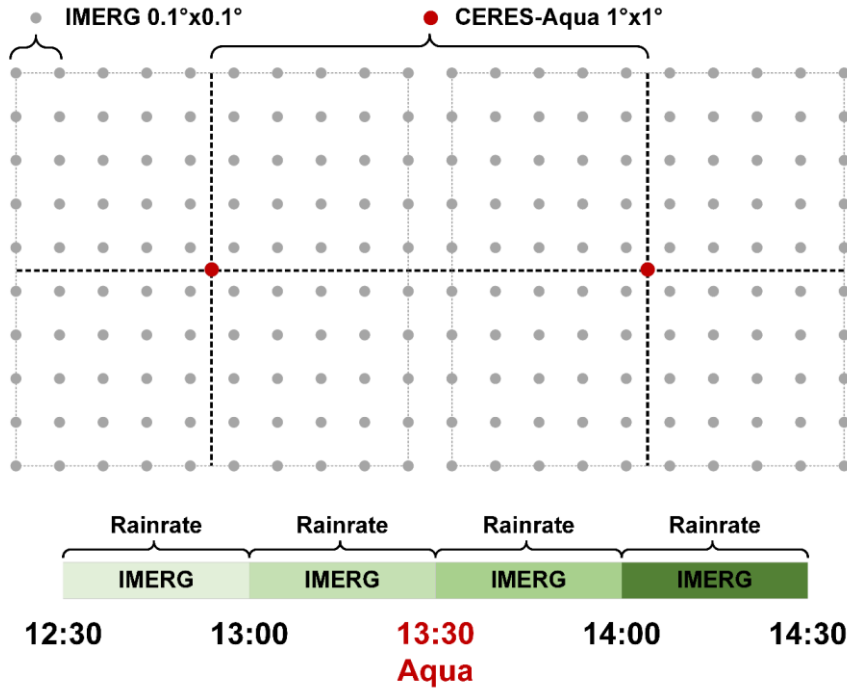
209 Precipitation data were obtained from the Integrated Multi-satellite Retrievals for GPM (IMERG)  
210 Version 07 Final run. IMERG is the flagship precipitation product of the Global Precipitation  
211 Measurement (GPM) mission, a collaborative effort between NASA and JAXA (Huffman et al., 2023).  
212 The IMERG algorithm calibrates, merges, and interpolates precipitation estimates from the constellation  
213 of Low Earth Orbit (LEO) passive microwave (PMW) radiometers onboard GPM satellites. These  
214 estimates are subsequently integrated with geostationary satellite infrared observations, particularly in  
215 regions with sparse PMW coverage, to produce a global precipitation product with  $0.1^\circ$  spatial and 30-  
216 minute temporal resolutions (Huffman et al., 2020; Watters et al., 2021). IMERG precipitation data,  
217 owing to its global coverage and high spatiotemporal resolution, have been widely adopted by the  
218 research community (Dezfuli et al., 2017; Durden, 2024; Hayden et al., 2023; Tan et al., 2019a; Watters  
219 et al., 2021; Watters and Battaglia, 2019; Zhang and Wang, 2024; Zhu et al., 2024). Consequently,  
220 IMERG V07 Final Run PrecipitationCal, the gauge-calibrated multi-satellite product, is used here to  
221 determine whether precipitation occurred within each CERES–MODIS grid cell.

## 222 **2.6 Data Quality Control**

223 To minimize the influence of satellite retrieval biases when investigating ACI, a rigorous quality-control  
224 procedure was applied to the CERES–MODIS cloud dataset following the method of Saponaro et al.  
225 (2017). The selection criteria were as follows:

- 226 1. Only liquid-phase warm clouds were retained, identified by a cloud-phase flag of “liquid” and CTT  
227  $> 273$  K.
- 228 2. To reduce the impact of large-scale cloud-macrophysical variability and highlight microphysical  
229 processes, only clouds with CTP between 650 and 950 hPa were selected.
- 230 3. Thin clouds with  $\tau < 5$  were excluded to minimize retrieval uncertainty.
- 231 4. A threshold of  $< 0.2$  mm  $\text{h}^{-1}$  was adopted to identify IMERG non-raining cases, following Tan et al.  
232 (2019b). The IMERG precipitation data were first collocated onto CERES–MODIS  $1^\circ \times 1^\circ$  grid  
233 cells. A grid cell was then classified as non-raining when all IMERG sub-pixels within the 13:00–

234 13:30 and 13:30–14:00 local time intervals recorded precipitation rates below  $0.2 \text{ mm h}^{-1}$ , as  
 235 illustrated in Fig. 2.



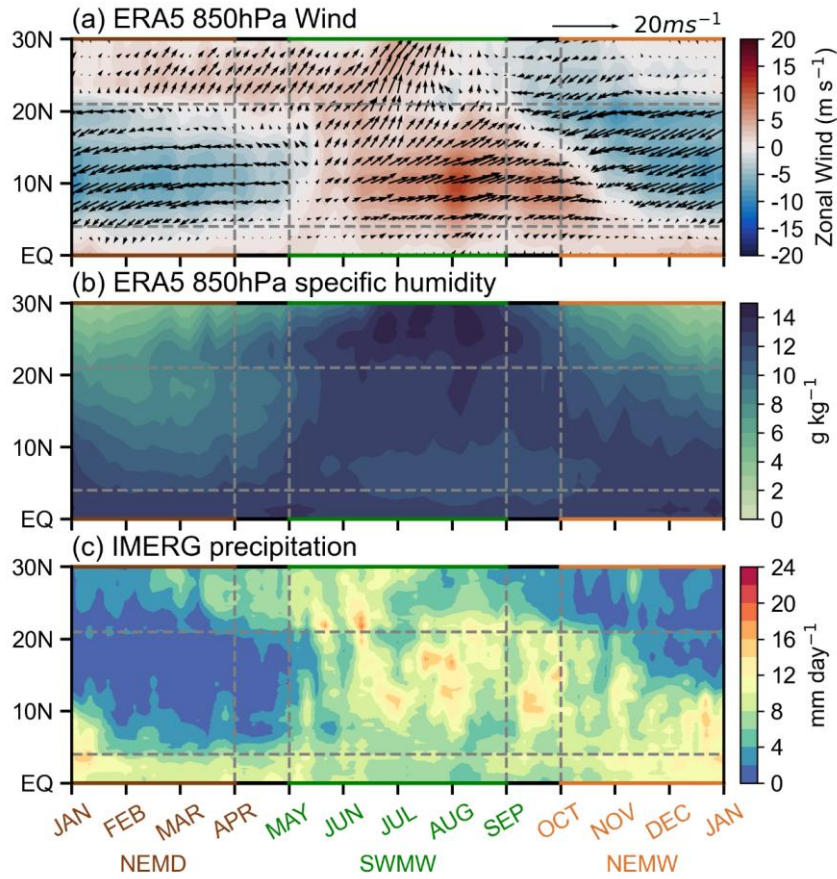
236  
 237 **Figure 2: Schematic illustration of the procedure used to identify non-raining CERES–MODIS grid cells**  
 238 **based on IMERG V07 Final Run PrecipitationCal.**

### 239 3 Result

#### 240 3.1 Definition of Monsoon Periods over the South China Sea

241 ACI are strongly modulated by environmental factors such as humidity, vertical wind velocity, and  
 242 atmospheric stability (Zhu et al., 2022). Therefore, considering the prevailing atmospheric conditions is  
 243 crucial when examining their variability. The atmospheric environment over the SCS exhibits distinct  
 244 characteristics under the influence of the southwest monsoon and the northeast monsoon. A distinctive  
 245 feature of the SCS summer monsoon is its nearly simultaneous onset across a broad latitudinal range  
 246 ( $3^{\circ}$ – $22^{\circ}$ N) (Wang et al., 2004). On top of the previous studies that defined monsoon periods over the  
 247 SCS based on wind direction (Wang et al., 2004, 2009), we further incorporated precipitation and specific  
 248 humidity within this  $3$ – $22^{\circ}$ N band (the red box in Fig. 1) to classify the study periods into three regimes:

249 the southwest monsoon wet period (SWMW), the northeast monsoon dry period (NEMD), and the  
250 northeast monsoon wet period (NEMW). As shown in Fig. 3, the SCS is dominated by the southwest  
251 monsoon from May to August, during which specific humidity reaches its maximum and precipitation is  
252 strongest. From October to December, the northeast monsoon prevails, accompanied by relatively high  
253 specific humidity and intense precipitation. During January to March, the SCS remains under the  
254 influence of the northeast monsoon, but specific humidity is at its lowest and precipitation is minimal,  
255 representing a dry period. Accordingly, we defined May–August as SWMW, October–December as  
256 NEMW, and January–March as NEMD. These three periods not only reflect significant differences in  
257 atmospheric circulation and moisture conditions, along with aerosol regimes over the SCS, but also  
258 provide distinct environmental backgrounds for ACI, which may influence their characteristics and  
259 intensity.



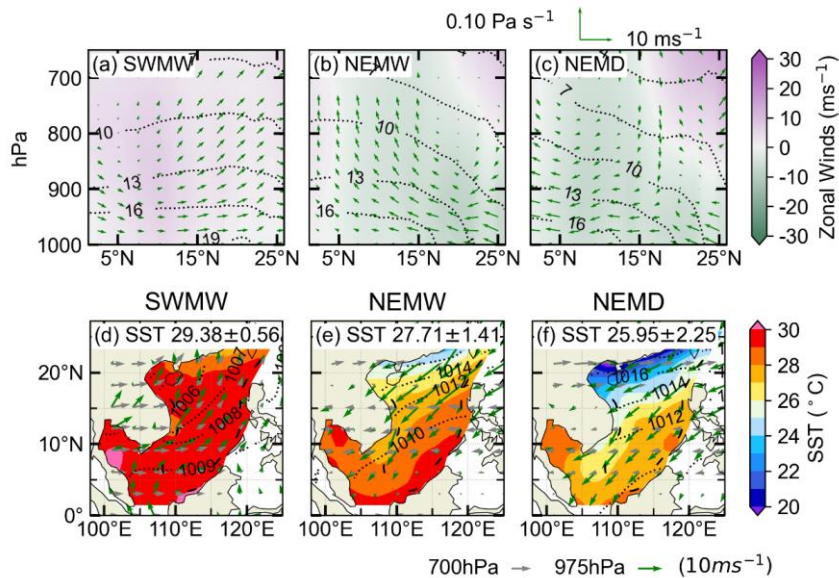
260  
 261 **Figure 3: Time–latitude distribution of the (a) ERA5 climatological pentad mean 850 hPa zonal wind (Jul**  
 262 **2002–Feb 2020) and (b) ERA5 pentad mean 850 hPa specific humidity (Jul 2002–Feb 2020) and (c) IMERG**  
 263 **pentad mean precipitation (Jul 2002–Feb 2020). The data are averaged over the longitude bands between**  
 264 **110E and 120E across the SCS. The arrows in (a) indicates 850hPa horizontal winds.**

### 265 3.2 Atmospheric conditions and Aerosol–Cloud properties during the Three Periods

#### 266 3.2.1 Atmospheric Circulation and Sea Surface Temperature

267 The Hadley circulation over the SCS is modulated by the Asian monsoon system and the seasonal  
 268 variation of solar radiation. Fig. 4a shows that during the SWMW period, the SCS is dominated by  
 269 ascending motion, which is associated with the presence of the Intertropical Convergence Zone (ITCZ)  
 270 over the region. During the NEMW period, the Hadley circulation shifts southward and the subtropical  
 271 high is established over the northern SCS (Fig. 4e). As a result, subsidence dominates the northern part

272 of the region, whereas ascending motion occurs over the equatorial southern part (Fig. 4b). During the  
 273 NEMD period, as the Hadley circulation continues to shift southward, the subtropical high dominates  
 274 the SCS (Fig. 4f), leading to prevailing subsidence over the region (Fig. 4c). As shown in Figs. 4a-c, the  
 275 water vapor content over the SCS gradually decreases from the SWMW period to the NEMW period and  
 276 further to the NEMD period. During the SWMW period, the winds over the SCS are predominantly  
 277 westerly. In contrast, during both the NEMW and NEMD periods, the winds are mainly easterly.  
 278 Additionally, a westerly jet is present at upper levels over the northern SCS. These features show that  
 279 the SCS exhibits distinct vertical circulation, moisture, and wind patterns under different monsoon  
 280 conditions.



281  
 282 **Fig. 4.** Zonally averaged cross section of the atmospheric circulation from ERA5 (Jul 2002–Feb 2020) for the  
 283 domain bounded between 110°E and 120°E during (a) the southwest monsoon wet period, (b) the northeast  
 284 monsoon wet period, and (c) the northeast monsoon dry period. Meridional and pressure velocity are denoted  
 285 by arrows (↑ indicates upward motion), whereas colors indicate the zonal wind component. Black contour is  
 286 specific humidity. Panels (d–f) show the corresponding overview of meteorological conditions and SST over  
 287 the SCS region. Color shades represent SST from OISST (Jul 2002–Feb 2020), black contour is sea level  
 288 pressure from ERA5 (Jul 2002–Feb 2020), and arrows are near-surface wind speed at 975 hPa (green) and  
 289 that at 700 hPa (gray) from ERA5 (Jul 2002–Feb 2020).

290 The SCS exhibits contrasting large-scale circulation patterns between the southwest and northeast  
 291 monsoon periods, as shown in Figs. 4d–f. During the SWMW period, the SCS is influenced by tropical

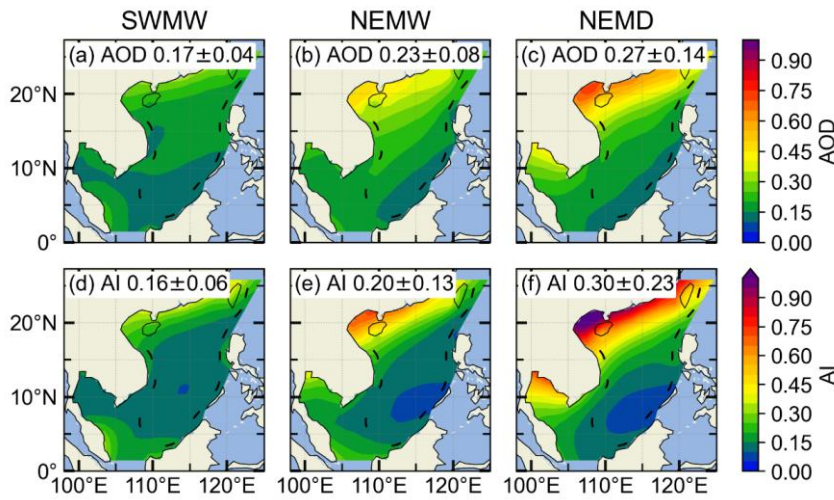
292 and equatorial maritime air masses, with prevailing southwesterlies over the region (Martin and  
293 Howland, 1982), whereas during the northeast monsoon, winter airflows originating from Siberia and  
294 the Mongolian Plateau result in prevailing northeasterlies (Liu et al., 2024). These opposite prevailing  
295 wind directions play a crucial role in modulating the transport pathways of continental pollutants into the  
296 SCS. Specifically, air masses originating from the Indochinese Peninsula and surrounding Southeast  
297 Asian land regions are the primary sources of pollutants transported into the SCS (Miller et al., 2023; Ou  
298 et al., 2025; Sun et al., 2023; Zhang et al., 2019), whereas during the northeast monsoon, continental  
299 emissions from China may be carried southward into the region (Xiao et al., 2017; Yuan et al., 2024;  
300 Zheng et al., 2023).

301 Figures 4d–f show that the area-averaged SST over the SCS is highest during the SWMW period ( $29.38$   
302  $\pm 0.56$  °C), lower during the NEMW period ( $27.71 \pm 1.41$  °C), and lowest during the NEMD period  
303 ( $25.95 \pm 2.25$  °C), with variations consistent with those of specific humidity. During the southwest  
304 monsoon, the SST gradient across the SCS is relatively small, whereas during the northeast monsoon,  
305 SST decreases with increasing latitude (Wu et al., 2020), and a cold water band forms along the coastal  
306 region near mainland China (Chen and Hu, 2023). Higher SST promotes strong latent and sensible heat  
307 fluxes, which in turn enhance the atmospheric moisture content over the region (Lee and Park, 2022;  
308 Zhang et al., 1995). Consequently, SST and atmospheric moisture exhibit consistent variations across  
309 the three periods. In addition, during the northeast monsoon, both the SST (Figs. 4e–f) and atmospheric  
310 moisture (Figs. 4b–c) decrease with increasing latitude, showing similar latitudinal gradients.

### 311 **3.2.2 Aerosol and cloud properties**

312 The area-averaged aerosol values over the SCS exhibit clear differences among the three periods (Fig.  
313 5). The lowest values occur during the SWMW period, with  $AOD = 0.17 \pm 0.04$  and  $AI = 0.16 \pm 0.06$ .  
314 Higher values are observed during the NEMW period, with  $AOD = 0.23 \pm 0.08$  and  $AI = 0.20 \pm 0.13$ ,  
315 whereas the NEMD period shows the highest values, with  $AOD = 0.27 \pm 0.14$  and  $AI = 0.30 \pm 0.23$ ,  
316 indicating different aerosol sources. Significant differences in aerosol distribution are also observed  
317 between the southwest and northeast periods. During the southwest period, higher aerosol values are  
318 found in the northern SCS near mainland China and in the southwestern SCS near Malaysia. During the  
319 northeast period, aerosol values exhibit a pronounced gradient, forming a coastal band that decreases

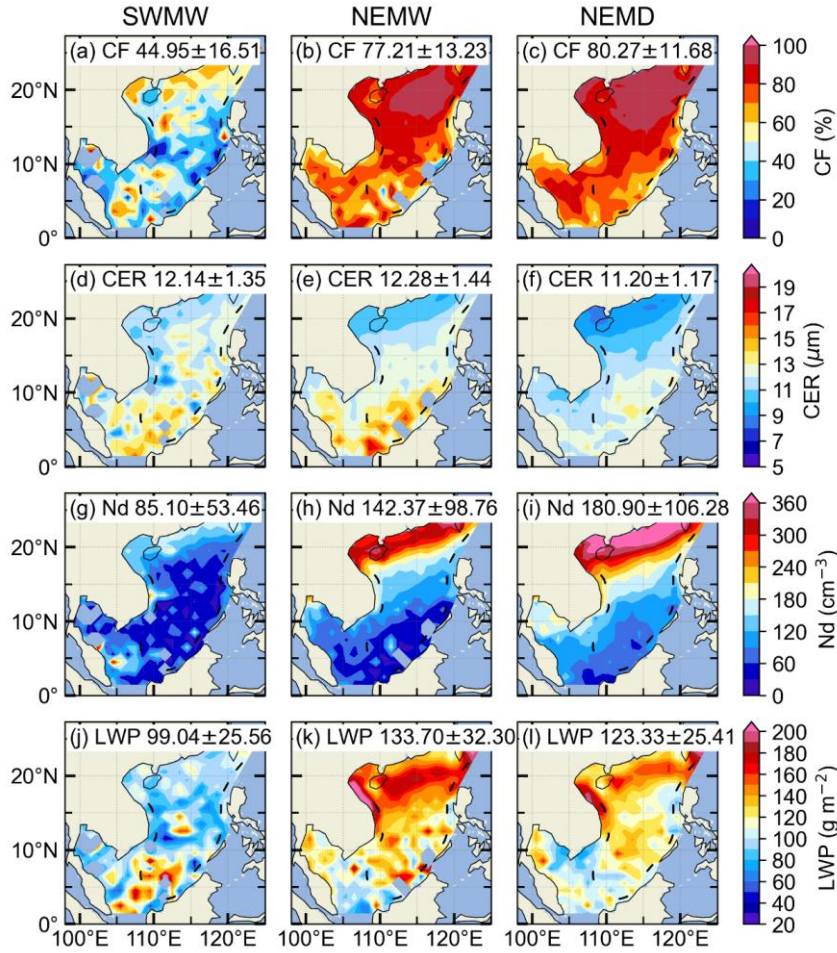
320 with increasing distance from the shoreline (Tu et al., 2021). Compared with AOD, AI incorporates  
 321 aerosol size information and is therefore considered a more suitable proxy for cloud condensation nuclei  
 322 in studies of ACI (Nakajima et al., 2001). Over the northern SCS near mainland China, AI values are  
 323 larger than AOD, indicating that aerosols in this region are dominated by fine particles. In contrast, in  
 324 the central SCS, farther from the continent, AI values are smaller than AOD, suggesting that aerosols  
 325 there are primarily coarse particles from natural sources.



326  
 327 **Figure 5: Spatial distributions of MERRA-2 AOD (Jul 2002–Feb 2020) over the South China Sea, averaged**  
 328 **over different periods: (a) the southwest monsoon wet period, (b) the northeast monsoon wet period, and (c)**  
 329 **the northeast monsoon dry period. (d–f) Corresponding AI (Jul 2002–Feb 2020) averaged over the same**  
 330 **periods.**

331 Figure 6 shows the variations in macrophysical and microphysical properties of warm clouds over the  
 332 SCS during the three monsoon periods. During the SWMW period, the area-averaged warm-cloud  
 333 fraction over the SCS is the lowest ( $44.95 \pm 16.51$  %), whereas comparable higher values are observed  
 334 during the NEMW ( $77.21 \pm 13.23$  %) and NEMD ( $80.27 \pm 11.68$  %) periods. Although the SCS  
 335 experiences the highest water vapor content during the SWMW period, the presence of strong updrafts  
 336 enhances cloud development (Fig. 4a), leading to the lowest fraction of warm clouds and an increased  
 337 occurrence of mixed-phase and ice clouds. During the northeast monsoon, the advection of dry and cold  
 338 continental air over the SCS likely suppresses convective activity, maintaining a higher fraction of warm  
 339 clouds in the region. Additionally, During the northeast monsoon, the fraction of warm clouds is highest

340 in the northern SCS, whereas lower values are observed in the southern region near the equator, likely  
 341 due to stronger convective activity in the equatorial area.



342  
 343 **Figure 6: Spatial distributions of warm-cloud (a–c) cloud fraction, (d–f) cloud droplet effective radius, (g–i)**  
 344 **cloud droplet number concentration, and (j–l) liquid water path over the South China Sea during the**  
 345 **southwest monsoon (first column), the northeast monsoon wet period (second column), and the northeast**  
 346 **monsoon dry period (third column).**

347 The area-averaged warm-cloud droplet effective radius over the SCS is similar across the three monsoon  
 348 periods, with values of  $12.14 \pm 1.35 \mu\text{m}$  during the SWMW period,  $12.28 \pm 1.54 \mu\text{m}$  during the NEMW  
 349 period, and  $11.20 \pm 1.17 \mu\text{m}$  during the NEMD period (Figs. 6d–f). In terms of the spatial distribution of  
 350 warm-cloud droplet effective radius, droplets near the equatorial region tend to be larger than those in

351 other areas, likely due to more pronounced droplet collision and coalescence driven by precipitation,  
352 which increases droplet size.

353 The area-averaged warm-cloud droplet number concentration over the SCS exhibits distinct differences  
354 among the three periods. The lowest mean value occurs during the SWMW period ( $85.10 \pm 53.46 \text{ cm}^{-3}$ ),  
355 followed by a higher value during the NEMW period ( $142.37 \pm 98.76 \text{ cm}^{-3}$ ), and the highest value during  
356 the NEMD period ( $180.90 \pm 106.28 \text{ cm}^{-3}$ ) (Figs. 6g–i). The highest cloud droplet number concentration  
357 is observed in the northern SCS adjacent to the Chinese mainland, showing a strong spatial  
358 correspondence with aerosol distribution. Aerosol concentrations are also largest in this region (Fig. 5),  
359 consistent with the Twomey effect, whereby enhanced aerosol loading increases cloud droplet number  
360 concentration. In the southern SCS near the equator, cloud droplet number concentration is relatively  
361 low, which may be attributed to lower aerosol concentrations and/or stronger convective activity that  
362 promotes droplet growth and reduces droplet number.

363 The area-averaged warm-cloud LWP over the SCS is lowest during the SWMW period ( $99.04 \pm 25.56 \text{ g}$   
364  $\text{m}^{-2}$ ), highest during the NEMW period ( $133.70 \pm 32.30 \text{ g m}^{-2}$ ), and intermediate during the NEMD period  
365 ( $123.21 \pm 25.41 \text{ g m}^{-2}$ ) (Figs. 6j–l). During the northeast monsoon, the highest LWP values are observed  
366 in the northern SCS adjacent to the Chinese mainland. This may be attributed to more polluted  
367 environments, where the second indirect aerosol effect suppresses precipitation, thereby leading to an  
368 increase in LWP (Albrecht, 1989). It is noteworthy that the LWP in the northern SCS is higher during  
369 the NEMW period than during the NEMD period, which may be associated with sedimentation-  
370 entrainment feedback (Ackerman et al., 2004) and/or evaporation-entrainment feedbacks (Dagan et al.,  
371 2017; Wang et al., 2003). Compared with the NEMW period, the NEMD period is characterized by  
372 higher cloud droplet number concentrations and smaller CER in this region (Fig. 6e, f, h, i). These two  
373 feedbacks describe how increased droplet number concentrations and reduced droplet sizes can enhance  
374 cloud-top entrainment and evaporation, ultimately leading to a reduction in LWP (Gryspeerd et al.,  
375 2019). Additionally, under drier conditions above cloud tops during the NEMD period, the  
376 sedimentation-entrainment feedback may be further amplified, resulting in a stronger reduction in LWP  
377 (Gryspeerd et al., 2019; Sato et al., 2018). During the SWMW, LWP is also relatively high in the  
378 southern SCS near the equator (Fig. 6j). In this region, CER is larger and  $N_d$  is lower (Figs. 6d, g), likely

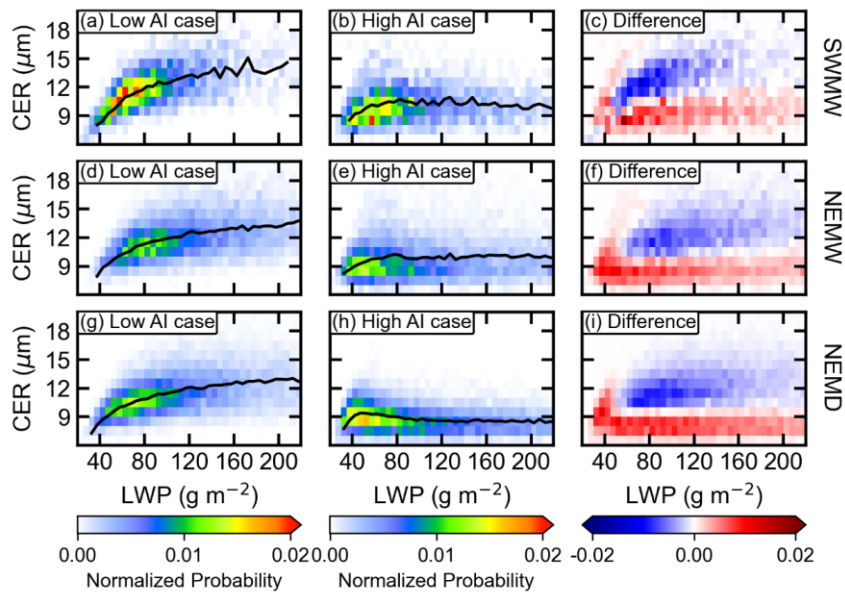
379 due to stronger updrafts near the equator, which enhance the vertical development of warm clouds and  
380 result in higher cloud water content.

381 Qualitatively, the consistency in zonal gradients of aerosol and cloud properties across all three monsoon  
382 regimes clearly reflects the theoretical ACI signal: aerosols increase  $N_d$  while reducing droplet size,  
383 which in turn lowers precipitation probability and thereby increases LWP and CF. Quantitatively,  
384 however, ACI intensities vary depending on the meteorological background (to be discussed in detail in  
385 the following section).

### 386 3.3 The Twomey Effect across the Three Periods

387 Twomey (1977) proposed that atmospheric aerosol particles can act as cloud condensation nuclei, such  
388 that an increase in aerosol loading leads to a higher cloud droplet number concentration. Under a nearly  
389 constant liquid water content, this results in smaller cloud droplet effective radius. To examine the  
390 Twomey effect during the three periods, the 25th and 75th percentiles of the AI were used to define clean  
391 ( $AI < 25$ th percentile) and polluted ( $AI > 75$ th percentile) conditions, respectively. For each condition,  
392 two-dimensional probability density distributions were calculated as a function of CER and LWP. The  
393 difference in the two-dimensional probability densities between polluted and clean conditions therefore  
394 illustrates how CER varies with aerosol loading under quasi-constant LWP. As shown in Fig. 7, CER is  
395 mostly smaller than  $15 \mu\text{m}$ , justifying the effectiveness of the filtering of non-raining cases. Under clean  
396 conditions, the CER of warm cloud increases with LWP across all three periods. Under polluted  
397 conditions, however, CER initially increases with LWP and then tends to level off during the SW period  
398 and the NEMW period. During the NEMD period, CER exhibits an increase followed by a decrease with  
399 increasing LWP, and subsequently remains nearly constant. The difference plots between polluted and  
400 clean conditions clearly demonstrate that polluted samples are more concentrated toward smaller CER  
401 values compared with clean samples in each quasi-constant LWP bin. This consistent shift toward  
402 smaller droplet sizes under higher aerosol loading demonstrates a clear manifestation of the Twomey  
403 effect during all three periods.

删除了:  $15\mu\text{m}$



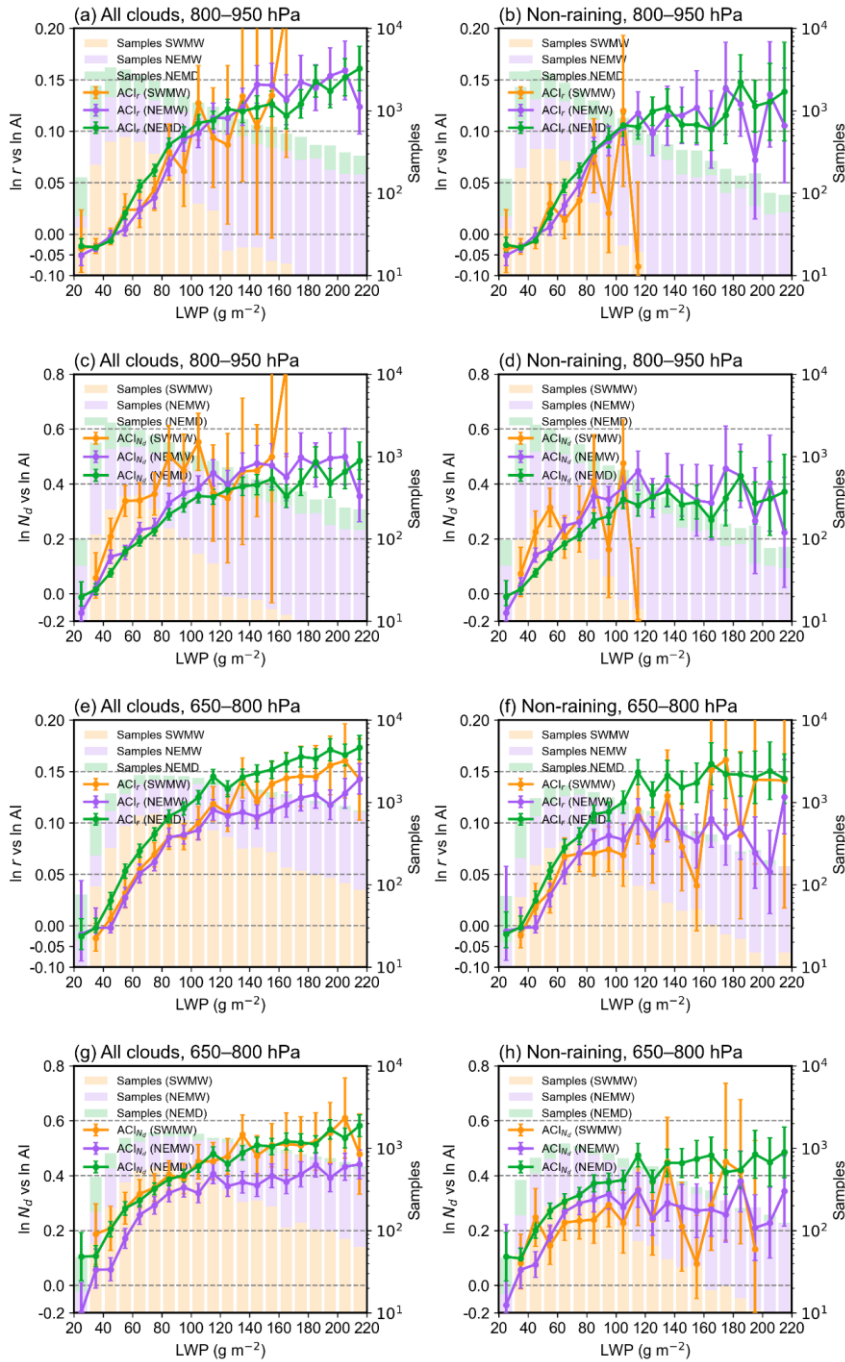
405

406 **Figure 7: Joint probability distributions of liquid water path (LWP) and cloud droplet effective radius (CER)**  
 407 **for warm clouds over the South China Sea during the three periods. The first, second, and third rows**  
 408 **correspond to the southwest monsoon, the northeast monsoon wet period, and the northeast monsoon dry**  
 409 **period, respectively. The first and second columns represent clean and polluted conditions, respectively. The**  
 410 **black lines denote the mean CER values within each LWP interval. The third column shows the differences**  
 411 **in probability density between polluted and clean conditions.**

### 412 3.4 Variations of ACI across the Three Periods

413 As shown in Fig. 6, the warm-cloud fraction during the Southwest Monsoon Wet period is approximately  
 414 45%, while it increases to about 77% during the Northeast Monsoon Wet period and further to about  
 415 80% during the Northeast Monsoon Dry period. This substantial difference suggests that the warm-cloud  
 416 populations sampled during different monsoon periods are fundamentally distinct and likely reflect  
 417 different cloud dynamical regimes. To better distinguish cloud morphological types within each monsoon  
 418 period and reduce potential regime-mixing effects, we further classified warm clouds over the SCS  
 419 according to CTP. Specifically, warm clouds were separated into shallow stratocumulus (CTP: 800–950  
 420 hPa) and deeper cumulus (CTP: 650–800 hPa) clouds. The ACI index were then quantified separately  
 421 for these two cloud regimes.

422 According to the assumption of the Twomey effect (Twomey, 1977), an essential prerequisite for  
423 investigating the aerosol indirect effect based on the CER–AI relationship is to keep the LWP constant.  
424 Since CER is a function of both LWP and AI, and generally increases with LWP, variations in LWP  
425 associated with changes in aerosols can in turn modulate the CER–AI relationship. Therefore, when  
426 applying the CER–AI relationship to analyse the first aerosol indirect effect, it is essential to constrain  
427 LWP to ensure its constancy. To satisfy this requirement while maintaining sufficient sample sizes, LWP  
428 was binned at  $10 \text{ g m}^{-2}$  intervals, within which  $\text{ACI}_r$  was examined separately for shallow stratocumulus  
429 (Fig. 8a-b) and deeper cumulus clouds (Fig. 8e-f) during the three periods. The results show that for both  
430 shallow stratocumulus and deeper cumulus clouds, under both all warm-cloud conditions and non-raining  
431 warm-cloud conditions,  $\text{ACI}_r$  is generally weak when  $\text{LWP} < 50 \text{ g m}^{-2}$ , and even exhibit the anti-Twomey  
432 effect (i.e., an increase in CER with increasing aerosol loading). Clouds in this LWP regime are typically  
433 very thin or broken, as well as post-precipitation remnants (McComiskey et al., 2009). A similar  
434 phenomenon is observed over the northern Indian Ocean, which may be attributed to the intense  
435 competition for available water vapor under high aerosol concentrations, combined with the entrainment  
436 of dry air at cloud tops (Jose et al., 2020). When  $\text{LWP} > 50 \text{ g m}^{-2}$ , the ACI for all cloud regimes across  
437 the three periods are consistent with the Twomey effect. An exception occurs in Fig. 8b and Fig. 8d,  
438 where the ACI at  $\text{LWP} = 120 \text{ g m}^{-2}$  during the southwest monsoon is negative. however, this result is not  
439 statistically robust due to the limited sample size.



441 **Figure 8: Linear regression slopes of  $\ln$  CER versus  $\ln$  AI and  $\ln$   $N_d$  versus  $\ln$  AI for shallow stratocumulus**  
442 **clouds (CTP = 800–950 hPa; a–d) and deeper cumulus clouds (CTP = 650–800 hPa; e–h) during the three**  
443 **periods. The first and second columns represent all cloud and non-raining cloud conditions, respectively.**  
444 **Green, purple, and yellow lines represent the southwest monsoon, northeast monsoon wet period, and**  
445 **northeast monsoon dry period, respectively. Error bars denote the 95 % confidence intervals of the linear**  
446 **regressions. Colored bars, consistent with the line colors, indicate the total number of samples within each**  
447 **LWP bin for the corresponding periods.**

448 Precipitation formation efficiently reduces cloud droplet number concentration and scavenges aerosols  
449 from clouds (Gryspeerd et al., 2015), introducing a sink of that does not reflect the Twomey effect (Jia et  
450 al., 2022). Therefore, when analyzing the aerosol first indirect effect in warm clouds, the influence of  
451 precipitation should be separated in order to accurately quantify the sensitivity of CER to aerosols. Fig.  
452 8 shows that, for both shallow stratocumulus and deeper cumulus clouds over the SCS, the  $ACI_r$  values  
453 for all warm cloud are consistently larger than those for non-raining warm-cloud across all three periods  
454 when LWP exceeds approximately  $80 \text{ g m}^{-2}$ . This indicates that the inclusion of raining samples amplifies  
455  $ACI_r$ , a phenomenon also identified in the AI/AOD– $N_d$  relationship by Jia et al. (2022) and Painemal et  
456 al. (2020). But this amplification is just an artifact governed by the joint impacts of the suppression of  
457 precipitation by aerosols and the aerosol removal by precipitation (Jia et al., 2022). Therefore, after  
458 removing precipitating clouds from all warm-cloud samples, the  $ACI_r$  obtained from non-raining warm  
459 clouds provides a more realistic representation. Nevertheless, the possibility of undetected light drizzle  
460 under high-LWP conditions may introduce additional uncertainty in the derived  $ACI$  estimates, despite  
461 precipitation screening using IMERG.

462 Fig. 8b. shows that, under non-raining warm-cloud conditions with  $LWP > 50 \text{ g m}^{-2}$ , the period-to-period  
463 variations in  $ACI_r$  differ between shallow stratocumulus and deeper cumulus clouds over the SCS. For  
464 shallow stratocumulus  $ACI_r$  values are broadly comparable across the three periods, with no significant  
465 differences (Fig. 8b). In contrast, deeper cumulus clouds exhibit clear differences among the three periods  
466 (Fig. 8f), with  $ACI_r$  generally strongest during the NEMD period, while the NEMW and SWMW periods  
467 show comparatively weaker values, with the NEMW period exceeding the SWMW period in some LWP  
468 bins. For  $LWP > 140 \text{ g m}^{-2}$ , the  $ACI_r$  during the southwest monsoon exhibits large fluctuations due to  
469 the limited number of samples, even exceeding that of the northeast monsoon. The analysis in Section  
470 3.2 reveals substantial differences in atmospheric conditions over the SCS among the three periods.

471 During the SWMW period, atmospheric moisture and sea surface temperatures reach their highest levels,  
472 and upward motion dominates over the region, while aerosol concentrations remain relatively low.  
473 During the NEMW period, moisture and sea surface temperatures are still relatively high, with upward  
474 motion primarily confined to the southern areas near the equator, and aerosol concentrations are elevated  
475 due to pollution transported from continental China. In contrast, during the NEMD period, atmospheric  
476 moisture and sea surface temperatures are at their lowest, subsidence dominates, and aerosol  
477 concentrations reach their maximum. These results suggest that although the large-scale environmental  
478 statistics differ substantially among the three monsoon periods, the local thermodynamic conditions  
479 favourable for shallow stratocumulus formation may be relatively similar across periods. Such cloud-  
480 favourable environments may not be fully resolved by the period-mean large-scale statistics presented  
481 here, which could explain the broadly comparable  $ACI_r$  values for shallow stratocumulus. In contrast,  
482  $ACI_r$  for deeper cumulus clouds over the SCS generally tends to strengthen under drier and more stable  
483 monsoon environments, with the strongest signals occurring during the NEMD period, while no  
484 consistent ordering is observed between the NEMW and SWMW periods across different LWP bins.  
485 Accordingly, the subsequent analysis focuses on the period-to-period differences of deeper cumulus  
486 clouds  $ACI$  and its relationship with variations in the monsoon environmental background.  
487 In addition to the radius-based  $ACI_r$ , we further examined the droplet-number susceptibility ( $ACI_{Nd}$ )  
488 separately for shallow stratocumulus (Fig. 8c–d) and deeper cumulus clouds (Fig. 8g–h). Consistent with  
489 the  $ACI_r$  results,  $ACI_{Nd}$  for shallow stratocumulus remains broadly comparable across the three monsoon  
490 periods, with no significant differences. Deeper cumulus clouds exhibit clear period-to-period variations,  
491 with the strongest signals occurring during the NEMD period, while comparatively weaker values are  
492 observed during the SWMW and NEMW periods. The consistency between  $ACI_r$  and  $ACI_{Nd}$  suggests  
493 that the  $ACI_r$  variations are robust to the choice of metric. However, because the two metrics are  
494 not independent, their agreement should be interpreted primarily as a consistency check rather than as  
495 independent evidence for the underlying physical mechanisms. Nevertheless, the similar inter-period  
496 variations exhibited by both metrics motivate a further examination of the environmental factors  
497 associated with these  $ACI$  differences. Therefore, Section 3.5 explores the potential influences of  
498 moisture and LTS on deeper cumulus cloud  $ACI$  across the three periods.

删除了: Such

删除了: highlights

删除了: observed period-to-period differences in

删除了: are governed by systematic changes in the underlying meteorological environment rather than by

删除了:  $ACI$

删除了: Motivated by this

删除了: investigates how variations in

删除了: regulate the evolution of

删除了: clouds

509 **3.5 Causes of ACI Variations across the Three Periods**

510 The progressive enhancement of  $ACI_r$  and  $ACI_{Nd}$  for deeper cumulus clouds from the SWMW to the  
511 NEMD period (Fig. 8) may potentially be influenced by the aerosol hygroscopic swelling artifact. The  
512 MERRA-2 AOD used to construct AI is calculated under ambient RH, with the extinction coefficients  
513 of sulfate, hydrophilic carbonaceous aerosols, and sea salt explicitly parameterized as functions of RH  
514 (Randles et al., 2017). Under humid conditions, aerosol hygroscopic growth can increase AOD, and  
515 therefore AI, without a corresponding increase in CCN-active particle number. This may artificially  
516 flatten the CER–AI and Nd–AI regression slopes, leading to apparently weaker ACI under moister  
517 conditions. Given that the SWMW and NEMW periods are characterized by substantially higher  
518 moisture levels than the NEMD period, the weaker ACI observed during these moister periods could  
519 partly reflect this hygroscopic swelling artifact rather than intrinsic differences in cloud microphysical  
520 sensitivity.

521 To assess whether the observed period-to-period differences are substantially affected by systematic  
522 humidity differences, we further stratified the data from each monsoon period into three RH ranges (0–  
523 45 %, 45–80 %, and 80–100 %). Under constrained LWP (50–200  $g\ m^{-2}$ ) and cloud-top pressure (650–  
524 800 hPa) conditions,  $ACI_{Nd}$  was recalculated separately for each subsample. The RH used in this study  
525 is from ERA5 at 950 hPa at 06:00 UTC, representing the ambient environmental humidity within the  
526 marine atmospheric boundary layer. Previous studies show that aerosols are predominantly confined  
527 below ~3 km in the marine atmosphere over the SCS (Li et al., 2020; Su et al., 2022), with a peak in  
528 extinction occurring at approximately ~480 m (Su et al., 2022). Therefore, the 950 hPa RH is adopted as  
529 a representative proxy for the ambient humidity governing aerosol hygroscopic growth.

530 As shown in Table 2, the enhancement from SWMW to NEMW and further to NEMD is evident in the  
531 moderate and high RH bins (45–80 % and 80–100 %), whereas the low RH bin (0–45 %) does not exhibit  
532 statistically robust differences among the three periods. These results suggest that although AI may be  
533 affected by hygroscopic swelling under humid environments, this effect is insufficient to explain the  
534 systematic ACI differences among the three monsoon periods. Therefore, aerosol hygroscopic swelling  
535 is unlikely to be the dominant cause of the observed period-to-period variability, motivating further  
536 examination of the thermodynamic and moisture controls on ACI.

删除了: all RH bins consistently exhibit the same

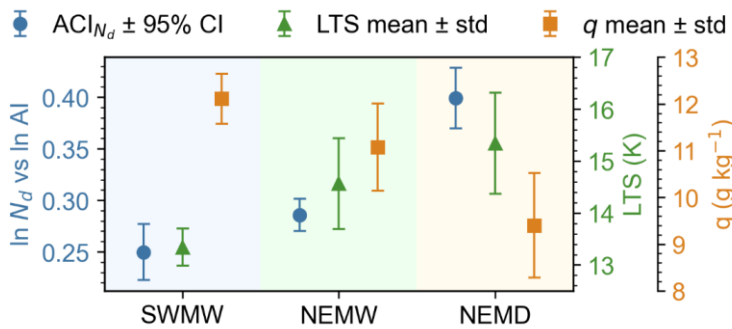
删除了: pattern

539 **Table 2:  $ACI_{Nd} \pm 95\%CI$  of deeper cumulus clouds under different relative humidity bins during the three**  
 540 **periods.**

Period	RH<45%	45% ≤ RH < 80%	80% ≤ RH ≤ 100%
SWMW	-0.126 ± 0.291	0.221 ± 0.043	0.278 ± 0.038
NEMW	-0.055 ± 0.194	0.262 ± 0.032	0.312 ± 0.018
NEMD	0.127 ± 0.102	0.371 ± 0.022	0.377 ± 0.012

541 To provide an integrated view of how the ACI of deeper cumulus clouds co-varies with the  
 542 thermodynamic and moisture background across the three periods, Fig. 9 shows the  $ACI_{Nd}$  together with  
 543 the corresponding  $q$  and  $LTS$ . Both  $ACI_{Nd}$  and the key environmental regulators display a coherent  
 544 evolution across the three periods. From the SWMW to the NEMW and NEMD,  $ACI_{Nd}$  intensify steadily,  
 545 in parallel with declining moisture and increasing  $LTS$ . Quantitatively, The  $ACI_{Nd}$  increases  
 546 progressively from  $0.250 \pm 0.027$  (95% confidence interval, 95% CI) during the SWMW period to  $0.286$   
 547  $\pm 0.016$  during NEMW and further to  $0.399 \pm 0.029$  during NEMD. Meanwhile,  $q$  decreases from  $12.111$   
 548  $\pm 0.540 \text{ g kg}^{-1}$  during SWMW to  $11.072 \pm 0.931 \text{ g kg}^{-1}$  during NEMW and  $9.540 \pm 1.120 \text{ g kg}^{-1}$  during  
 549 NEMD, while the  $LTS$  increases from  $13.341 \pm 0.358 \text{ K}$  to  $14.565 \pm 0.875 \text{ K}$  and  $15.343 \pm 0.977 \text{ K}$ ,  
 550 respectively. (All  $q$  and  $LTS$  uncertainties represent one standard deviation, std.) These co-varying  
 551 changes indicate that both  $q$  and  $LTS$  may regulate the strengthening of ACI across the three periods  
 552 over the SCS. In the following subsections, we separately examine the roles of  $q$  (Section 3.5.1) and  $LTS$   
 553 (Section 3.5.2) in regulating ACI.

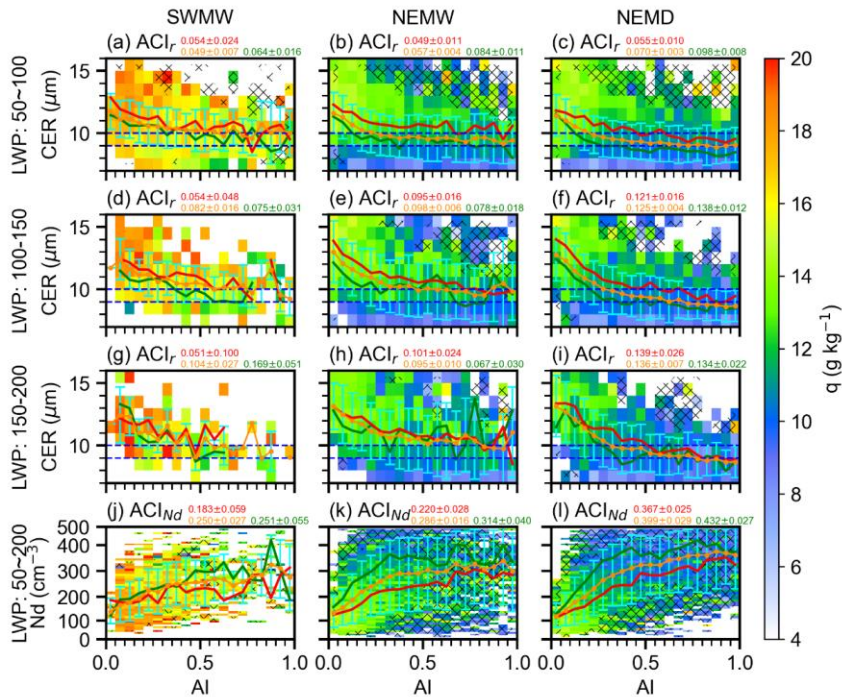
删除了: LST



554 **Figure 9:  $ACI_{Nd}$ , specific humidity ( $q$ ), and lower-tropospheric stability ( $LTS$ ) for the three periods over the**  
 555 **South China Sea. The 95% confidence interval (CI) represents the uncertainty derived from the Student's t**  
 556 **test, whereas std denotes the one standard deviation.**  
 557

559 **3.5.1 Water vapor**

560 Water vapor supply substantially impacts CCN activation, droplet condensational growth, and  
561 coalescence, hence altering the cloud droplet size distribution (Feingold et al., 2006; Zheng et al., 2022).  
562 Specific humidity at 1000 hPa serves as a proxy for the ambient water vapor available to warm clouds,  
563 analogous to the use of near-surface specific humidity as a proxy for marine boundary layer moisture in  
564 previous studies (Dadashazar et al., 2020). To investigate the influence of water vapor on ACI in deeper  
565 cumulus clouds, specific humidity was averaged within each AI-CER/ $N_d$  interval separately for each  
566 period (Fig. 10). For each AI interval, CER/ $N_d$  was further averaged, and samples were stratified by the  
567 25th and 75th percentiles of specific humidity to represent dry (< 25th percentile) and moist (> 75th  
568 percentile) conditions, under which the corresponding mean CER/ $N_d$  was calculated. In addition, ACI  
569 was derived from all samples and separately for the dry and moist subsets in each period. To satisfy the  
570 LWP constraint required for the CER-AI analysis, the influence of water vapor on ACI was examined  
571 within LWP intervals of 50–100, 100–150, and 150–200 g m<sup>-2</sup>. In addition, because the  $N_d$ -AI  
572 relationship does not require an explicit LWP constraint for ACI <sub>$N_d$</sub>  calculation, it was examined over the  
573 broader LWP range of 50–200 g m<sup>-2</sup>.



574

575 **Figure 10: Influence of water vapor on ACI in deeper cumulus clouds (CTP: 650-800 hPa) across the three**  
 576 **periods. Rows 1–3 show mean specific humidity in CER–AI bins for LWP ranges of 50–100, 100–150, and**  
 577 **150–200 g m<sup>-2</sup>, respectively; row 4 shows mean specific humidity in N<sub>d</sub>-AI bins for LWP 50–200 g m<sup>-2</sup>.**  
 578 **Columns correspond to the southwest monsoon, northeast monsoon wet period, and northeast monsoon dry**  
 579 **period. Yellow dashed, red, and green lines denote the mean CER (rows 1–3) or N<sub>d</sub> (row 4) in each AI bin for**  
 580 **all samples, for moist conditions (specific humidity > 75th percentile), and for dry conditions (specific**  
 581 **humidity < 25th percentile), respectively. Error bars indicate the standard deviation of CER (rows 1–3) or**  
 582 **N<sub>d</sub> (row 4) within each AI bin. Yellow numbers indicate ACI ± 95% uncertainty estimates (according to a**  
 583 **Student’s t test) for all samples, whereas red and green numbers indicate the corresponding estimates under**  
 584 **moist and dry conditions, respectively.**

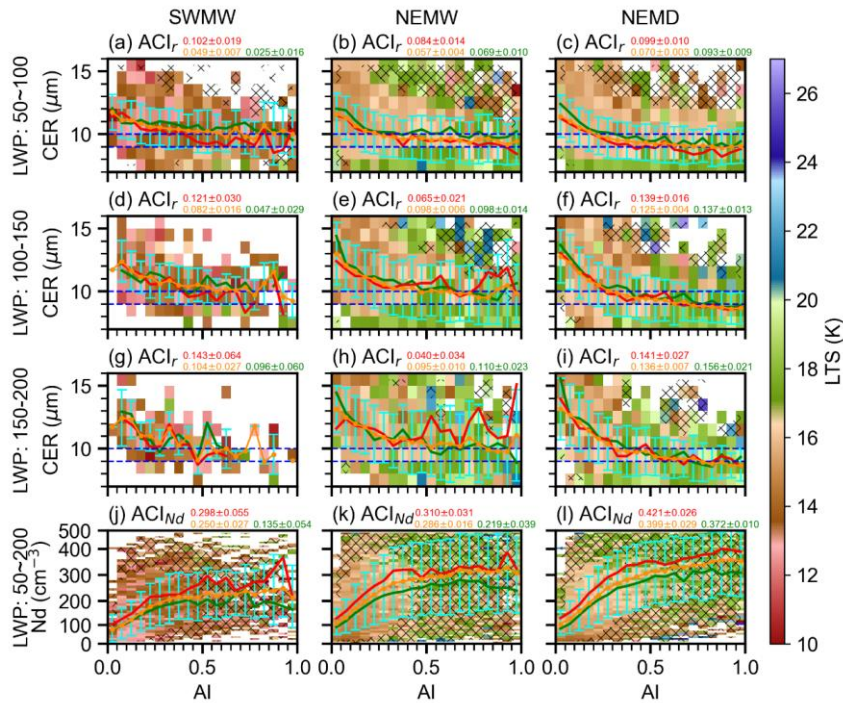
585 As shown in Fig. 10, higher specific humidity conditions are generally associated with larger CER and  
 586 lower N<sub>d</sub> across the three periods over the SCS. This may suggest that abundant water vapor enhances  
 587 condensational growth of cloud droplets, and the enlarged droplets are more susceptible to collision-  
 588 coalescence, which not only reduces Nd but also further increases the CER. By contrast, under limited  
 589 water vapor availability, the ability of CCN-activated droplets to grow by condensation is substantially  
 590 constrained. The lack of a sufficient number of larger droplets favors condensation as the predominant  
 591 growth mechanism, thereby yielding smaller droplet sizes (Zheng et al., 2022).

592 The response of ACI to environmental water availability exhibits different behaviors. Qiu et al. (2017)  
593 analysed the AI-CER relationship for non-raining warm clouds over the Southern Great Plains and found  
594 the anti-Twomey effect under moist conditions. Zheng et al. (2022) investigated non-raining warm  
595 clouds over the Eastern North Atlantic and found that sufficient water vapor availability can enhance  
596 ACI. Over the SCS, within the LWP range of 50–200 g m<sup>-2</sup>, ACI<sub>Nd</sub> is consistently smaller under moist  
597 conditions than under dry conditions across all three periods (Figs. 10j–l), suggesting that N<sub>d</sub> exhibits  
598 weaker sensitivity to aerosol perturbations in moist environments compared to dry environments. Figs.  
599 10j–l show that N<sub>d</sub> exhibits comparable values between moist and dry conditions at very low aerosol  
600 loading. As aerosol concentration increases, however, N<sub>d</sub> becomes smaller under moist conditions  
601 relative to dry conditions. This pattern may indicate that under ample water vapor availability, increased  
602 aerosol loading initially enhances cloud droplet activation, leading to elevated droplet number  
603 concentrations. But subsequent collision-coalescence promotes droplet growth while reducing N<sub>d</sub>.  
604 Consequently, the microphysical adjustments associated with enhanced moisture availability dampen the  
605 sensitivities of N<sub>d</sub> to aerosol perturbations, manifesting as weaker ACI<sub>Nd</sub> in the moist regime.  
606 In contrast, the response of ACI<sub>r</sub> to moisture exhibits a dependence on LWP. At low LWP (50–100 g m<sup>-2</sup>)  
607 <sup>2</sup>, ACI<sub>r</sub> is reduced under moist relative to dry conditions across all periods (Figs. 10a–c). At higher LWP  
608 ranges, this reduction appears only in the Southwest Monsoon period within the 100–150 g m<sup>-2</sup> and 150–  
609 200 g m<sup>-2</sup> bins, and in the Northeast Monsoon Dry period within the 100–150 g m<sup>-2</sup> bin (Fig. 10g), while  
610 the opposite response is observed in other cases. The LWP is defined as the column-integrated liquid  
611 water content within clouds (e.g., existing cloud droplets) (Lee and Penner, 2011). At low LWP, ACI<sub>r</sub> is  
612 weaker under moist conditions (as indicated by 1000-hPa specific humidity) compared to dry conditions  
613 (Figs. 10a–c). A possible explanation is that in moist environments, enhanced collision-coalescence  
614 processes promote droplet growth, leading to larger CER. In contrast, under drier conditions, limited  
615 water vapor availability inhibits droplet growth, resulting in smaller CER. At higher LWP, when the in-  
616 cloud liquid water content is abundant, the response of ACI<sub>r</sub> to environmental water vapor variations  
617 becomes less consistent (Figs. 10d–i), suggesting the involvement of additional microphysical or  
618 dynamical processes.

619 Over the SCS, CER and Nd exhibit comparable values across the three periods within the same LWP  
620 interval at low AI. As AI increases, noticeable differences develop, with CER decreasing progressively  
621 from the SW to the NEMW and further to the NEMD, while Nd increases accordingly (Fig. 10).  
622 Consequently, ACI is enhanced stepwise from SW to NEMW and then to NEMD. This stepwise  
623 enhancement may be partly attributed to the progressive decrease in environmental water vapor from  
624 SW to NEMW and further to NEMD (Figs. 4a–c), particularly evident within the LWP interval of 50–  
625 100 g m<sup>-2</sup>.

### 626 **3.5.2 lower tropospheric stability**

627 Thermodynamic and dynamic conditions are key factors influencing aerosol vertical transport, aerosol  
628 activation processes, and cloud droplet formation. Thermodynamic stability can be quantitatively  
629 represented by the lower tropospheric stability (LTS), a measure of temperature inversion strength  
630 initially defined for marine stratocumulus clouds (Klein and Hartmann, 1993). This metric has been  
631 widely utilized to evaluate atmospheric stability and vertical mixing across both oceanic and continental  
632 regions (Jia et al., 2019; Ma et al., 2018b). Higher LTS values represent enhanced lower tropospheric  
633 stability, which suppresses vertical mixing and convective initiation. To further examine the influence of  
634 thermodynamic conditions on ACI in deeper cumulus clouds, the LTS was analysed in a manner identical  
635 to that used for specific humidity. For each period, samples were stratified by the 25th and 75th  
636 percentiles of LTS to represent unstable and stable conditions, respectively, and ACI was computed for  
637 each subset (Fig. 11). The analysis was performed within LWP intervals of 50–100, 100–150, and 150–  
638 200 g m<sup>-2</sup> for the CER–AI relationship, and over 50–200 g m<sup>-2</sup> for the Nd–AI relationship. Fig. 11 shows  
639 that stronger lower tropospheric stability (higher LTS) is associated with smaller CER and higher Nd, as  
640 enhanced static stability may suppresses convective mixing and vertical moisture transport, thereby  
641 limiting droplet growth while favouring higher droplet concentrations.



642

643 **Figure 11: Same as Fig. 10, but for lower tropospheric stability. Stable and unstable conditions correspond to**  
 644 **the upper (> 75th percentile) and lower (< 25th percentile) quartiles of LTS, respectively. Yellow numbers**  
 645 **indicate  $ACI \pm 95\%$  uncertainty estimates (according to a Student's t test) for all samples, whereas red and**  
 646 **green numbers indicate the corresponding estimates under stable and unstable conditions, respectively.**

647 In contrast to unstable conditions, stronger  $ACI_{Nd}$  is observed under stable conditions characterized by  
 648 higher LTS values (Figs. 11j–l). This suggests that enhanced LTS may be associated with environmental  
 649 conditions that influence ACI. Under more stable stratification, reduced vertical mixing may help  
 650 maintain higher aerosol concentrations and moisture within the boundary layer, which may in turn  
 651 influence cloud droplet activation and cloud microphysical properties. As a result, higher  $ACI_{Nd}$  is  
 652 observed under stable conditions, compared to unstable environments. Over the SCS, LTS is generally  
 653 weaker during the southwest monsoon than during the northeast monsoon (Fig. 11), which may partly  
 654 contribute to the observed inter-monsoon differences in ACI. However, given the complexity of  
 655 concurrent variations in moisture, aerosol loading, and cloud regimes, the specific role of LTS in  
 656 modulating ACI cannot be isolated.

删除了: result

删除了: facilitate aerosol accumulation and coagulation, leading to an increase in aerosol particle size. Larger particles are more efficient on acting as CCN, thereby promoting cloud droplet activation and formation. The suppressed vertical mixing

删除了: further confine aerosols

删除了: strengthening local ACI. Consequently, the sensitivity of Nd to aerosol perturbations is enhanced

删除了: , manifesting as higher  $ACI_{Nd}$  relative

删除了: 11). The stronger atmospheric stability associated with the northeast ...

删除了: favors enhanced ACI

删除了: warm clouds, resulting

删除了: stronger

删除了: during the NE compared with the SW

672 The response of  $ACI_r$  to LTS exhibits distinct behaviours across different LWP intervals and periods  
 673 (Figs. 11a–i). During the southwest monsoon period,  $ACI_r$  is consistently larger under stable conditions  
 674 than under unstable conditions across all three LWP ranges, consistent with the  $ACI_{Nd}$  results. However,  
 675 during the northeast monsoon wet period, this enhancement is only evident in the lowest LWP range  
 676 ( $50\text{--}100\text{ g m}^{-2}$ ). In the northeast monsoon dry period, the enhancement under stable conditions is  
 677 observed in both the  $50\text{--}100\text{ g m}^{-2}$  and  $100\text{--}150\text{ g m}^{-2}$  bins. This contrasting behaviour (Figs. 11e, h, i)  
 678 can be further understood from the AI-CER relationships. At low AI values, corresponding to relatively  
 679 clean conditions, CER is larger under unstable conditions than under stable conditions. As AI increases,  
 680 indicating more polluted environments, CER under stable and unstable conditions gradually converges,  
 681 leading to stronger  $ACI_r$  under unstable conditions. This pattern may indicate that during the northeast  
 682 monsoon period, when in-cloud water vapor is abundant and aerosol loading is relatively high, cloud  
 683 microphysical processes become less sensitive to variations in LTS. The inherently strong and weakly  
 684 variable lower-tropospheric stability during the northeast monsoon may suppress the dynamical  
 685 influence of further LTS changes  $ACI_r$ , thereby weakening the LTS dependence of  $ACI_r$  under moist and  
 686 polluted conditions.

#### 687 4 discussion and conclusions

688 To investigate how  $ACI_r$  vary under the alternating influence of two opposing monsoon systems over the  
 689 South China Sea (SCS) and how different environmental conditions modulate these interactions, the  
 690 study period was divided into three representative phases based on variations in wind direction,  
 691 precipitation, and specific humidity: the southwest monsoon wet period (SWMW), the northeast  
 692 monsoon wet period (NEMW), and the northeast monsoon dry period (NEMD). Satellite observations  
 693 and reanalysis data were used to quantify  $ACI_r$  variability and its environmental controls across different  
 694 thermodynamic and moisture conditions.  
 695 Distinct environmental regimes characterize the three monsoon phases. SWMW is dominated by strong  
 696 ascent, high SST, and abundant moisture. NEMW features enhanced continental aerosol transport,  
 697 reduced SST, and increased LTS. NEMD is the driest and most stable regime, with widespread  
 698 subsidence and favourable conditions for boundary-layer aerosol accumulation.

删除了: (SW

删除了: By integrating

删除了: and satellite observations, this study examined the variations in

删除了: the associated

删除了: controlling factors during these three periods. The main findings are summarized as follows:

删除了: 1. SCS exhibits distinct seasonal

删除了: conditions associated with

删除了: prevailing

删除了: regimes. During the SW, the SCS

删除了: upward motion

删除了: SSTs

删除了: atmospheric

删除了: During the

删除了: .

删除了: outflow transports aerosols over the SCS while SSTs decrease...

删除了: strengthens; ascent

删除了: largely confined to the equatorial south

删除了: moisture remains relatively high. During the NEMD, continental influence persists but the environment becomes drier and more...

删除了: the lowest SSTs and

删除了: , favouring the

删除了: of fine-mode aerosols. These contrasting meteorological and environmental conditions among the SW, NEMW, and NEMD periods establish a distinct seasonal background over the SCS and exert a decisive influence on  $ACI_r$

728 A pronounced Twomey effect was consistently identified across all three periods, as indicated by smaller  
729 CER and higher Nd with increasing aerosol loading under nearly constant LWP. Quantitative estimates  
730 of  $ACI_r$  show that the Twomey effect dominates when LWP ranges from 50 to 200 g m<sup>-2</sup>, whereas an  
731 apparent “anti-Twomey” behaviour appears in optically thin clouds ( $LWP < 50 \text{ g m}^{-2}$ ), likely associated  
732 with strong competition for limited water vapor and entrainment-induced drying. Precipitation tends to  
733 amplify the ACI by simultaneously suppressing cloud droplet number concentrations and removing  
734 aerosols from the atmosphere. After removing raining samples, the ACI derived from non-raining warm  
735 clouds provides a more reliable representation of the first aerosol indirect effect, reducing biases caused  
736 by precipitation processes, although some uncertainty may remain due to undetected light precipitation  
737 under high-LWP conditions. Across the three periods, shallow stratocumulus clouds (CTP: 800–950 hPa)  
738 show limited variability in ACI, while deeper cumulus clouds (CTP: 650–800 hPa) exhibit the strongest  
739 ACI during NEMD. In contrast, no clear separation is observed between the SWMW and NEMW  
740 periods.  
741 The inter-monsoon differences in deeper cumulus cloud ACI are primarily governed by coupled  
742 variations in moisture, atmospheric stability, and aerosol conditions rather than monsoon phase itself.  
743 Stronger ACI in NEMD is consistent with drier and more stable conditions that favour aerosol  
744 accumulation and suggests a possible role of aerosol accumulation in increasing aerosol availability for  
745 cloud activation, which may in turn contribute to stronger ACI. In contrast, moist and convectively active  
746 environments during SWMW and NEMW likely weaken ACI through enhanced condensational and  
747 coalescence growth processes. These results highlight the key role of environmental modulation in  
748 shaping the expression of the Twomey effect in marine warm clouds over the SCS.  
749 Uncertainties arise from the use of AI as a proxy for CCN, which does not fully capture coarse-mode  
750 sea-salt aerosols, potential biases associated with aerosol hygroscopic growth, and assumptions in Nd  
751 retrieval (e.g., constant sub-adiabatic factor). Cloud selection criteria may preferentially retain more  
752 homogeneous scenes, potentially underrepresenting broken cumulus clouds, and may be less reliable for  
753 deeper trade cumulus and congestus clouds that dominate the 650–800 hPa CTP regime highlighted in  
754 this study. Undetected light precipitation may also affect ACI estimates, especially at high LWP. In  
755 addition, the present analysis cannot fully disentangle the respective influences of water vapor,

删除了: 2.

删除了: exceeds

删除了: .

删除了: a

删除了: increase from

删除了: to

删除了: and further to NEMD, reaching a maximum in NEMD

删除了: 3. Environmental conditions exert a strong influence on deeper cumulus cloud ACI intensity over the SCS. Water vapor availability may play a critical role in regulating cloud droplet activation and growth.  $ACI_{Nd}$  is consistently smaller under moist conditions than under dry conditions across all three periods, indicating that Nd exhibits weaker sensitivity to aerosol perturbations in moist environments compared to dry environments. Thermodynamic stability may also modulate ACI variability.  $ACI_{Nd}$  is generally enhanced under stable atmospheric conditions, as stronger LTS may suppress vertical mixing and confine aerosols and moisture within the boundary layer, thereby facilitating aerosol accumulation and potentially promoting CCN activation. Overall, deeper cumulus cloud ACI tends to be more pronounced in dry and stable environments, which are typical of the NEMD, and weakest under moist and convectively active environments during the SWMW. However, these conclusions should be treated with caution, as...

780 thermodynamic stability, cloud regime, and aerosol type and loading, as these factors co-vary  
781 systematically with the monsoon phase, which limits attribution of the observed inter-period ACI  
782 differences to any single controlling mechanism.

783 Despite these uncertainties, the results show that deeper cumulus cloud ACI over the SCS are strongly  
784 regulated by coupled variations in moisture, stability, and aerosol conditions associated with monsoon  
785 transitions. Monsoon phases act not as direct physical drivers but as an organizing framework for  
786 environmental variability that shapes cloud microphysical responses. Future work will focus on reducing  
787 observational and retrieval uncertainties to improve the quantification of ACI across different monsoon  
788 regimes. These findings provide important observational evidence for understanding ACI and offer  
789 valuable guidance for improving the representation of ACI in climate and numerical weather prediction  
790 models.

#### 792 Financial support

793 This work was supported by the National Natural Science Foundation of China (grant nos. 42027804,  
794 41775026, and 41075012). Hailing Jia was support by the project ACIaction (File No.  
795 OCENW.M.24.024) financed by the Dutch Research Council (NWO) under the grant  
796 <https://doi.org/10.61686/OZRJI30024>.

#### 798 Acknowledgements

799 Data and samples were collected onboard of R/V Shiyang 6 implementing the open research cruise  
800 NORC2024-07 supported by NSFC Shiptime Sharing Project (project number: 42349907). And we  
801 sincerely appreciate the valuable comments provided by the two anonymous reviewers, which  
802 significantly enhanced the clarity and robustness of this work.

#### 804 Competing Interest

805 The authors declare that they have no known competing financial interests or personal relationships that  
806 could have appeared to influence the work reported in this paper.

807

删除了: . These

删除了: It is worth noting

删除了: the use of AI as a CCN proxy may be affected by aerosol hygroscopic swelling, introducing additional uncertainty in the period-to-period variations of

删除了: . However, a consistent increasing tendency across the three periods is still observed within all relative humidity bins, indicating that the inter-period differences are

删除了: primarily driven by hygroscopic swelling effects,

删除了: are more likely controlled by systematic changes in the

删除了: conditions.¶

In addition, the coexistence of sea-salt coarse-mode and anthropogenic fine-mode aerosols over the South China Sea introduces uncertainty in using AI as a CCN proxy, particularly due to its limited representation of giant CCN associated with sea salt. This may weaken the diagnosed Twomey effect and introduce additional uncertainty in ACI estimates.

删除了: explicitly separating aerosol types to better quantify their respective roles in cloud microphysical processes during

删除了: periods.¶

Furthermore, the Nd retrieval assumes a constant sub-adiabatic factor ( $f_{ad} = 0.8$ ), which may introduce a systematic offset in Nd estimation (Gryspeerd et al., 2022). Such an assumption may vary in validity under different meteorological conditions and could potentially introduce seasonal biases, thereby affecting the magnitude of the derived ACI and the inter-period ACI gradient.¶

Overall, deeper cumulus cloud ACI increases from SW to NEMW and further to NEMD, consistent with co-varying decreases in moisture and increases in atmospheric stability. However, the simultaneous variation of moisture, stability, cloud regime, and aerosol loading across monsoon phases limits the attribution of their individual contributions to the observed inter-period differences.

删除了: results highlight that the coupling among aerosols, moisture, and thermodynamic stability exerts fundamental control over marine warm-cloud microphysical processes in tropical monsoon regions. The

844 Author contributions

845 YL analysed the data and wrote the manuscript. HJ participated in scientific discussions and reviewed  
846 and refined the manuscript. YH participated in scientific discussions, and Resources, Project  
847 administration, Funding acquisition, Conceptualization, Formal analysis, Methodology, Writing –  
848 review & editing.

849

850 Data Availability

851 Atmospheric fields were obtained from the ERA5 reanalysis datasets produced by the European Centre  
852 for Medium-Range Weather Forecasts (ECMWF) via the Copernicus Climate Change Service (C3S)  
853 Climate Data Store (CDS). The data are publicly available at <https://cds.climate.copernicus.eu/>.

854 Aerosol datasets were obtained from the Modern-Era Retrospective Analysis for Research and  
855 Applications Version 2 (MERRA-2), produced by the NASA Goddard Earth Observing System (GEOS)  
856 Global Modeling and Assimilation Office (GMAO) and distributed by the Goddard Earth Sciences Data  
857 and Information Services Center (GES DISC). The data are publicly available at  
858 <https://disc.gsfc.nasa.gov/datasets?project=MERRA-2>.

859 Cloud retrievals were obtained from the Clouds and the Earth's Radiant Energy System (CERES)-  
860 Moderate Resolution Imaging Spectroradiometer (MODIS) Edition 4 Single Scanner Footprint (SSF)  
861 daily Level-3 products ( $1^\circ \times 1^\circ$  grid), produced by NASA's Langley Research Center (LaRC) and  
862 distributed by the Atmospheric Science Data Center (ASDC). The CERES–MODIS data are publicly  
863 available through the NASA ASDC archive at <https://ceres.larc.nasa.gov/data/#ssf1deg-level-3>.

864 [Cloud droplet number concentration data are from Gryspeerd et al. \(2022\) MODIS-based product \( \$1^\circ \times\$   
865  \$1^\circ\$ \), available at <https://dx.doi.org/10.5285/864a46cc65054008857ee5bb772a2a2b>](https://doi.org/10.5285/864a46cc65054008857ee5bb772a2a2b)

866 Sea surface temperature (SST) data were obtained from the National Oceanic and Atmospheric  
867 Administration (NOAA) Optimum Interpolation (OI) SST, Version 2, produced by the NOAA Physical  
868 Sciences Laboratory. The data are publicly available through the NOAA Physical Sciences Laboratory  
869 at <https://psl.noaa.gov/data/gridded/data.noaa.oisst.v2.html>.

870 IMERG V07 precipitation data used in this study are openly available from the NASA Goddard Earth  
871 Sciences Data and Information Services Center (GES DISC) at  
872 <https://disc.gsfc.nasa.gov/datasets?keywords=gpm%20imerg%2007>, as cited in Huffman et al. (2024).

873

#### 874 **References**

875 Ackerman, A. S., Kirkpatrick, M. P., Stevens, D. E., and Toon, O. B.: The impact of humidity above  
876 stratiform clouds on indirect aerosol climate forcing, *Nature*, 432, 1014–1017,  
877 <https://doi.org/10.1038/nature03174>, 2004.

878 Albrecht, B. A.: Aerosols, Cloud Microphysics, and Fractional Cloudiness, *Science*, 245, 1227–1230,  
879 1989.

880 Bellouin, N., Quaas, J., Gryspeerdt, E., Kinne, S., Stier, P., Watson-Parris, D., Boucher, O., Carslaw, K.  
881 S., Christensen, M., Daniau, A.-L., Dufresne, J.-L., Feingold, G., Fiedler, S., Forster, P., Gettelman, A.,  
882 Haywood, J. M., Lohmann, U., Malavelle, F., Mauritsen, T., McCoy, D. T., Myhre, G., Mülmenstädt, J.,  
883 Neubauer, D., Possner, A., Rugenstein, M., Sato, Y., Schulz, M., Schwartz, S. E., Sourdeval, O.,  
884 Storelvmo, T., Toll, V., Winker, D., and Stevens, B.: Bounding Global Aerosol Radiative Forcing of  
885 Climate Change, *Reviews of Geophysics*, 58, e2019RG000660, <https://doi.org/10.1029/2019RG000660>,  
886 2020.

887 Chen, J. and Hu, Z.: Seasonal variability in spatial patterns of sea surface cold- and warm fronts over the  
888 continental shelf of the northern South China Sea, *Front. Mar. Sci.*, 9,  
889 <https://doi.org/10.3389/fmars.2022.1100772>, 2023.

890 Chen, Y., Luo, T., Sun, G., Zhu, W., Liu, Q., Liu, Y., Jin, X., and Weng, N.: A Comprehensive Ensemble  
891 Model for Marine Atmospheric Boundary-Layer Prediction in Meteorologically Sparse and Complex  
892 Regions: A Case Study in the South China Sea, *Remote Sensing*, 17, 2046,  
893 <https://doi.org/10.3390/rs17122046>, 2025.

894 Chen, Y.-C., Christensen, M. W., Stephens, G. L., and Seinfeld, J. H.: Satellite-based estimate of global  
895 aerosol–cloud radiative forcing by marine warm clouds, *Nature Geosci*, 7, 643–646,  
896 <https://doi.org/10.1038/ngeo2214>, 2014.

897 Costantino, L. and Bréon, F.-M.: Aerosol indirect effect on warm clouds over South-East Atlantic, from  
898 co-located MODIS and CALIPSO observations, *Atmospheric Chemistry and Physics*, 13, 69–88,  
899 <https://doi.org/10.5194/acp-13-69-2013>, 2013.

900 Dadashazar, H., Crosbie, E., Majdi, M. S., Panahi, M., Moghaddam, M. A., Behrangī, A., Brunke, M.,  
901 Zeng, X., Jonsson, H. H., and Sorooshian, A.: Stratocumulus cloud clearings: statistics from satellites,

902 reanalysis models, and airborne measurements, *Atmos Chem Phys*, 20, 4637–4665,  
903 <https://doi.org/10.5194/acp-20-4637-2020>, 2020.

904 Dagan, G., Koren, I., Altaratz, O., and Heiblum, R. H.: Time-dependent, non-monotonic response of  
905 warm convective cloud fields to changes in aerosol loading, *Atmospheric Chemistry and Physics*, 17,  
906 7435–7444, <https://doi.org/10.5194/acp-17-7435-2017>, 2017.

907 Dezfuli, A. K., Ichoku, C. M., Huffman, G. J., Mohr, K. I., Selker, J. S., Van De Giesen, N.,  
908 Hochreutener, R., and Annor, F. O.: Validation of IMERG Precipitation in Africa, *Journal of*  
909 *Hydrometeorology*, 18, 2817–2825, <https://doi.org/10.1175/JHM-D-17-0139.1>, 2017.

910 Douglas, A. and L’Ecuyer, T.: Quantifying variations in shortwave aerosol–cloud–radiation interactions  
911 using local meteorology and cloud state constraints, *Atmospheric Chemistry and Physics*, 19, 6251–  
912 6268, <https://doi.org/10.5194/acp-19-6251-2019>, 2019.

913 Douville, H., Raghavan, K., Renwick, J., Allan, R. P., Arias, P. A., Barlow, M., Cerezo-Mota, R.,  
914 Cherchi, A., Gan, T. Y., and Gergis, J.: *Climate Change 2021 – The Physical Science Basis: Working*  
915 *Group I Contribution to the Sixth Assessment Report of the Intergovernmental Panel on Climate Change*,  
916 1st ed., Cambridge University Press, <https://doi.org/10.1017/9781009157896>, 2023.

917 Durden, S. L.: Evaluation of IMERG Data over Open Ocean Using Observations of Tropical Cyclones,  
918 *Remote Sensing*, 16, 2028, <https://doi.org/10.3390/rs16112028>, 2024.

919 Fan, J., Yuan, T., Comstock, J. M., Ghan, S., Khain, A., Leung, L. R., Li, Z., Martins, V. J., and  
920 Ovchinnikov, M.: Dominant role by vertical wind shear in regulating aerosol effects on deep convective  
921 clouds, *Journal of Geophysical Research: Atmospheres*, 114, <https://doi.org/10.1029/2009JD012352>,  
922 2009.

923 Fan, J., Wang, Y., Rosenfeld, D., and Liu, X.: Review of Aerosol–Cloud Interactions: Mechanisms,  
924 Significance, and Challenges, <https://doi.org/10.1175/JAS-D-16-0037.1>, 2016.

925 Feingold, G., Remer, L. A., Ramaprasad, J., and Kaufman, Y. J.: Analysis of smoke impact on clouds in  
926 Brazilian biomass burning regions: An extension of Twomey’s approach, *J. Geophys. Res.*, 106, 22907–  
927 22922, <https://doi.org/10.1029/2001JD000732>, 2001.

928 Feingold, G., Furrer, R., Pilewskie, P., Remer, L. A., Min, Q., and Jonsson, H.: Aerosol indirect effect  
929 studies at Southern Great Plains during the May 2003 Intensive Operations Period, *Journal of*  
930 *Geophysical Research: Atmospheres*, 111, <https://doi.org/10.1029/2004JD005648>, 2006.

931 Gelaro, R., McCarty, W., Suárez, M. J., Todling, R., Molod, A., Takacs, L., Randles, C. A., Darmenov,  
932 A., Bosilovich, M. G., Reichle, R., Wargan, K., Coy, L., Cullather, R., Draper, C., Akella, S., Buchard,  
933 V., Conaty, A., Silva, A. M. da, Gu, W., Kim, G.-K., Koster, R., Lucchesi, R., Merkova, D., Nielsen, J.  
934 E., Partyka, G., Pawson, S., Putman, W., Rienecker, M., Schubert, S. D., Sienkiewicz, M., and Zhao, B.:  
935 *The Modern-Era Retrospective Analysis for Research and Applications, Version 2 (MERRA-2)*,  
936 <https://doi.org/10.1175/JCLI-D-16-0758.1>, 2017.

937 Grosvenor, D. P., Sourdeval, O., Zuidema, P., Ackerman, A., Alexandrov, M. D., Bennartz, R., Boers,  
938 R., Cairns, B., Chiu, J. C., Christensen, M., Deneke, H., Diamond, M., Feingold, G., Fridlind, A.,  
939 Hünerbein, A., Knist, C., Kollias, P., Marshak, A., McCoy, D., Merk, D., Painemal, D., Rausch, J.,  
940 Rosenfeld, D., Russchenberg, H., Seifert, P., Sinclair, K., Stier, P., van Diedenhoven, B., Wendisch, M.,  
941 Werner, F., Wood, R., Zhang, Z., and Quaas, J.: Remote Sensing of Droplet Number Concentration in  
942 Warm Clouds: A Review of the Current State of Knowledge and Perspectives, *Reviews of Geophysics*,  
943 56, 409–453, <https://doi.org/10.1029/2017RG000593>, 2018.

944 Gryspeerdt, E., Stier, P., White, B. A., and Kipling, Z.: Wet scavenging limits the detection of aerosol  
945 effects on precipitation, *Atmospheric Chemistry and Physics*, 15, 7557–7570,  
946 <https://doi.org/10.5194/acp-15-7557-2015>, 2015.

947 Gryspeerdt, E., Goren, T., Sourdeval, O., Quaas, J., Mülmenstädt, J., Dipu, S., Unglaub, C., Gettelman,  
948 A., and Christensen, M.: Constraining the aerosol influence on cloud liquid water path, *Atmospheric  
949 Chemistry and Physics*, 19, 5331–5347, <https://doi.org/10.5194/acp-19-5331-2019>, 2019.

950 Gryspeerdt, E., McCoy, D. T., Crosbie, E., Moore, R. H., Nott, G. J., Painemal, D., Small-Griswold, J.,  
951 Sorooshian, A., and Ziemba, L.: The impact of sampling strategy on the cloud droplet number  
952 concentration estimated from satellite data, *Atmospheric Measurement Techniques*, 15, 3875–3892,  
953 <https://doi.org/10.5194/amt-15-3875-2022>, 2022.

954 Hayden, L. J. M., Tan, J., Bolvin, D. T., and Huffman, G. J.: Variations in the Diurnal Cycle of  
955 Precipitation and Its Changes with Distance from Shore over Two Contrasting Regions as Observed by  
956 IMERG, ERA5, and Spaceborne Ku Radar, *Journal of Hydrometeorology*, 24, 675–689,  
957 <https://doi.org/10.1175/JHM-D-22-0154.1>, 2023.

958 Hersbach, H., Bell, B., Berrisford, P., Hirahara, S., Horányi, A., Muñoz-Sabater, J., Nicolas, J., Peubey,  
959 C., Radu, R., Schepers, D., Simmons, A., Soci, C., Abdalla, S., Abellan, X., Balsamo, G., Bechtold, P.,  
960 Biavati, G., Bidlot, J., Bonavita, M., De Chiara, G., Dahlgren, P., Dee, D., Diamantakis, M., Dragani, R.,  
961 Flemming, J., Forbes, R., Fuentes, M., Geer, A., Haimberger, L., Healy, S., Hogan, R. J., Hólm, E.,  
962 Janisková, M., Keeley, S., Laloyaux, P., Lopez, P., Lupu, C., Radnoti, G., De Rosnay, P., Rozum, I.,  
963 Vamborg, F., Villaume, S., and Thépaut, J.: The ERA5 global reanalysis, *Quart J Royal Meteor Soc*,  
964 146, 1999–2049, <https://doi.org/10.1002/qj.3803>, 2020.

965 Huffman, G. J., Bolvin, D. T., Braithwaite, D., Hsu, K.-L., Joyce, R. J., Kidd, C., Nelkin, E. J.,  
966 Sorooshian, S., Stocker, E. F., Tan, J., Wolff, D. B., and Xie, P.: Integrated Multi-satellite Retrievals for  
967 the Global Precipitation Measurement (GPM) Mission (IMERG), in: *Satellite Precipitation  
968 Measurement*, vol. 67, edited by: Levizzani, V., Kidd, C., Kirschbaum, D. B., Kummerow, C. D.,  
969 Nakamura, K., and Turk, F. J., Springer International Publishing, Cham, 343–353,  
970 [https://doi.org/10.1007/978-3-030-24568-9\\_19](https://doi.org/10.1007/978-3-030-24568-9_19), 2020.

971 Huffman, G. J., Bolvin, D. T., Braithwaite, D., Hsu, K., Joyce, R., Kidd, C., Nelkin, E., Sorooshian, S.,  
972 Tan, J., and Xie, P.: NASA Global Precipitation Measurement (GPM) Integrated Multi-Satellite

973 Retrievals for GPM (IMERG) Version 07, Algorithm Theoretical Basis Document (ATBD) Version, 47,  
974 2023.

975 Jia, H. and Quaas, J.: Nonlinearity of the cloud response postpones climate penalty of mitigating air  
976 pollution in polluted regions, *Nat. Clim. Chang.*, 13, 943–950, [https://doi.org/10.1038/s41558-023-](https://doi.org/10.1038/s41558-023-01775-5)  
977 [01775-5](https://doi.org/10.1038/s41558-023-01775-5), 2023.

978 Jia, H., Ma, X., Quaas, J., Yin, Y., and Qiu, T.: Is positive correlation between cloud droplet effective  
979 radius and aerosol optical depth over land due to retrieval artifacts or real physical processes?, *Atmos.*  
980 *Chem. Phys.*, 19, 8879–8896, <https://doi.org/10.5194/acp-19-8879-2019>, 2019.

981 Jia, H., Ma, X., Yu, F., and Quaas, J.: Significant underestimation of radiative forcing by aerosol–cloud  
982 interactions derived from satellite-based methods, *Nat Commun*, 12, 3649,  
983 <https://doi.org/10.1038/s41467-021-23888-1>, 2021.

984 Jia, H., Quaas, J., Gryspeerdt, E., Böhm, C., and Sourdeval, O.: Addressing the difficulties in quantifying  
985 droplet number response to aerosol from satellite observations, *Atmospheric Chemistry and Physics*, 22,  
986 7353–7372, <https://doi.org/10.5194/acp-22-7353-2022>, 2022.

987 Jia, H., Hasekamp, O., and Quaas, J.: Revisiting Aerosol–Cloud Interactions From Weekly Cycles,  
988 *Geophysical Research Letters*, 51, <https://doi.org/10.1029/2024gl1108266>, 2024.

989 Jose, S., Nair, V. S., and Babu, S. S.: Anthropogenic emissions from South Asia reverses the aerosol  
990 indirect effect over the northern Indian Ocean, *Sci Rep*, 10, 18360, [https://doi.org/10.1038/s41598-020-](https://doi.org/10.1038/s41598-020-74897-x)  
991 [74897-x](https://doi.org/10.1038/s41598-020-74897-x), 2020.

992 Kim, B.-G., Schwartz, S. E., Miller, M. A., and Min, Q.: Effective radius of cloud droplets by ground-  
993 based remote sensing: Relationship to aerosol, *Journal of Geophysical Research: Atmospheres*, 108,  
994 <https://doi.org/10.1029/2003JD003721>, 2003.

995 Klein, S. A. and Hartmann, D. L.: *The Seasonal Cycle of Low Stratiform Clouds*, 1993.

996 Lee, S. S. and Penner, J. E.: Dependence of aerosol–cloud interactions in stratocumulus clouds on liquid-  
997 water path, *Atmospheric Environment*, 45, 6337–6346, <https://doi.org/10.1016/j.atmosenv.2011.08.050>,  
998 2011.

999 Lee, T.-W. and Park, J. E.: Thermodynamic correlations between the sea surface temperature, water  
1000 vapor content, and cloud fraction, using MODIS data, *Theor Appl Climatol*, 150, 1699–1706,  
1001 <https://doi.org/10.1007/s00704-022-04261-8>, 2022.

1002 [Li, Y., Wang, B., Lee, S.-Y., Zhang, Z., Wang, Y., and Dong, W.: Micro-Pulse Lidar Cruising](https://doi.org/10.3390/rs12101695)  
1003 [Measurements in Northern South China Sea, \*Remote Sensing\*, 12, <https://doi.org/10.3390/rs12101695>,](https://doi.org/10.3390/rs12101695)  
1004 [2020.](https://doi.org/10.3390/rs12101695)

1005 Liu, J., Yu, J., Lin, C., He, M., Liu, H., Wang, W., and Min, M.: Near-real-time atmospheric and oceanic  
1006 science products of Himawari-8 and Himawari-9 geostationary satellites over the South China Sea, *Earth*  
1007 *System Science Data*, 16, 4949–4969, <https://doi.org/10.5194/essd-16-4949-2024>, 2024.

1008 Ma, P.-L., Rasch, P. J., Chepfer, H., Winker, D. M., and Ghan, S. J.: Observational constraint on cloud  
1009 susceptibility weakened by aerosol retrieval limitations, *Nat Commun*, 9, 2640,  
1010 <https://doi.org/10.1038/s41467-018-05028-4>, 2018a.

1011 Ma, X., Jia, H., Yu, F., and Quaas, J.: Opposite Aerosol Index-Cloud Droplet Effective Radius  
1012 Correlations Over Major Industrial Regions and Their Adjacent Oceans, *Geophysical Research Letters*,  
1013 45, 5771–5778, <https://doi.org/10.1029/2018GL077562>, 2018b.

1014 Martin, D. W. and Howland, M. R.: Rainfall over the Arabian Sea during the onset of the 1979 monsoon,  
1015 *Nature*, 300, 628–630, <https://doi.org/10.1038/300628a0>, 1982.

1016 McComiskey, A., Feingold, G., Frisch, A. S., Turner, D. D., Miller, M. A., Chiu, J. C., Min, Q., and  
1017 Ogren, J. A.: An assessment of aerosol-cloud interactions in marine stratus clouds based on surface  
1018 remote sensing, *J. Geophys. Res.*, 114, 2008JD011006, <https://doi.org/10.1029/2008JD011006>, 2009.

1019 Miller, R. M., Rauber, R. M., Di Girolamo, L., Rilloraza, M., Fu, D., McFarquhar, G. M., Nesbitt, S. W.,  
1020 Ziemba, L. D., Woods, S., and Thornhill, K. L.: Influence of natural and anthropogenic aerosols on cloud  
1021 base droplet size distributions in clouds over the South China Sea and West Pacific, *Atmospheric*  
1022 *Chemistry and Physics*, 23, 8959–8977, <https://doi.org/10.5194/acp-23-8959-2023>, 2023.

1023 Minnis, P., Sun-Mack, S., Young, D. F., Heck, P. W., Garber, D. P., Chen, Y., Spangenberg, D. A.,  
1024 Arduini, R. F., Trepte, Q. Z., Smith, W. L., Ayers, J. K., Gibson, S. C., Miller, W. F., Hong, G.,  
1025 Chakrapani, V., Takano, Y., Liou, K.-N., Xie, Y., and Yang, P.: CERES Edition-2 Cloud Property  
1026 Retrievals Using TRMM VIRS and Terra and Aqua MODIS Data—Part I: Algorithms, *IEEE*  
1027 *Transactions on Geoscience and Remote Sensing*, 49, 4374–4400,  
1028 <https://doi.org/10.1109/TGRS.2011.2144601>, 2011a.

1029 Minnis, P., Sun-Mack, S., Chen, Y., Khaiyer, M. M., Yi, Y., Ayers, J. K., Brown, R. R., Dong, X.,  
1030 Gibson, S. C., Heck, P. W., Lin, B., Nordeen, M. L., Nguyen, L., Palikonda, R., Smith, W. L.,  
1031 Spangenberg, D. A., Trepte, Q. Z., and Xi, B.: CERES Edition-2 Cloud Property Retrievals Using  
1032 TRMM VIRS and Terra and Aqua MODIS Data—Part II: Examples of Average Results and  
1033 Comparisons With Other Data, *IEEE Transactions on Geoscience and Remote Sensing*, 49, 4401–4430,  
1034 <https://doi.org/10.1109/TGRS.2011.2144602>, 2011b.

1035 Minnis, P., Sun-Mack, S., Chen, Y., Chang, F.-L., Yost, C. R., Smith, W. L., Heck, P. W., Arduini, R.,  
1036 F., Bedka, S. T., Yi, Y., Hong, G., Jin, Z., Painemal, D., Palikonda, R., Scarino, B. R., Spangenberg, D.  
1037 A., Smith, R. A., Trepte, Q. Z., Yang, P., and Xie, Y.: CERES MODIS Cloud Product Retrievals for  
1038 Edition 4—Part I: Algorithm Changes, *IEEE Transactions on Geoscience and Remote Sensing*, 59,  
1039 2744–2780, <https://doi.org/10.1109/TGRS.2020.3008866>, 2021.

- 1040 Nakajima, T., Higurashi, A., Kawamoto, K., and Penner, J. E.: A possible correlation between satellite-  
1041 derived cloud and aerosol microphysical parameters, *Geophysical Research Letters*, 28, 1171–1174,  
1042 <https://doi.org/10.1029/2000GL012186>, 2001.
- 1043 Ou, H., Cai, M., Zhang, Y., Ni, X., Liang, B., Sun, Q., Mai, S., Sun, C., Zhou, S., Wang, H., Sun, J., and  
1044 Zhao, J.: Measurement report: Cloud condensation nuclei (CCN) activity in the South China Sea from  
1045 shipborne observations during the summer and winter of 2021 – seasonal variation and anthropogenic  
1046 influence, *Atmospheric Chemistry and Physics*, 25, 2495–2513, [https://doi.org/10.5194/acp-25-2495-](https://doi.org/10.5194/acp-25-2495-2025)  
1047 2025, 2025.
- 1048 Painemal, D.: Global estimates of changes in shortwave low-cloud albedo and fluxes due to variations  
1049 in cloud droplet number concentration derived from CERES-MODIS satellite sensors, *Geophys Res Lett*,  
1050 45, 9288–9296, <https://doi.org/10.1029/2018GL078880>, 2018.
- 1051 Painemal, D., Chang, F.-L., Ferrare, R., Burton, S., Li, Z., Smith Jr., W. L., Minnis, P., Feng, Y., and  
1052 Clayton, M.: Reducing uncertainties in satellite estimates of aerosol–cloud interactions over the  
1053 subtropical ocean by integrating vertically resolved aerosol observations, *Atmospheric Chemistry and*  
1054 *Physics*, 20, 7167–7177, <https://doi.org/10.5194/acp-20-7167-2020>, 2020.
- 1055 Peng, S., Zhu, Y., Huang, K., Ding, X., Shi, R., Wu, D., Feng, Y., and Wang, D.: Detecting the structure  
1056 of marine atmospheric boundary layer over the Northern South China Sea by shipboard GPS sondes,  
1057 *Atmospheric Science Letters*, 17, 564–568, <https://doi.org/10.1002/asl.693>, 2016.
- 1058 Qiu, Y., Zhao, C., Guo, J., and Li, J.: 8-Year ground-based observational analysis about the seasonal  
1059 variation of the aerosol-cloud droplet effective radius relationship at SGP site, *Atmospheric*  
1060 *Environment*, 164, 139–146, <https://doi.org/10.1016/j.atmosenv.2017.06.002>, 2017.
- 1061 Randles, C. A., Silva, A. M. da, Buchard, V., Colarco, P. R., Darmenov, A., Govindaraju, R., Smirnov,  
1062 A., Holben, B., Ferrare, R., Hair, J., Shinzuka, Y., and Flynn, C. J.: The MERRA-2 Aerosol Reanalysis,  
1063 1980 Onward. Part I: System Description and Data Assimilation Evaluation,  
1064 <https://doi.org/10.1175/JCLI-D-16-0609.1>, 2017.
- 1065 Reynolds, R. W., Rayner, N. A., Smith, T. M., Stokes, D. C., and Wang, W.: An Improved In Situ and  
1066 Satellite SST Analysis for Climate, 2002.
- 1067 Rosenfeld, D., Zhu, Y., Wang, M., Zheng, Y., Goren, T., and Yu, S.: Aerosol-driven droplet  
1068 concentrations dominate coverage and water of oceanic low-level clouds, *Science*, 363, eaav0566,  
1069 <https://doi.org/10.1126/science.aav0566>, 2019.
- 1070 Saponaro, G., Kolmonen, P., Sogacheva, L., Rodriguez, E., Virtanen, T., and De Leeuw, G.: Estimates  
1071 of the aerosol indirect effect over the Baltic Sea region derived from 12 years of MODIS observations,  
1072 *Atmos. Chem. Phys.*, 17, 3133–3143, <https://doi.org/10.5194/acp-17-3133-2017>, 2017.

- 1073 Sato, Y., Goto, D., Michibata, T., Suzuki, K., Takemura, T., Tomita, H., and Nakajima, T.: Aerosol  
1074 effects on cloud water amounts were successfully simulated by a global cloud-system resolving model,  
1075 *Nat Commun*, 9, 985, <https://doi.org/10.1038/s41467-018-03379-6>, 2018.
- 1076 Seinfeld, J. H., Bretherton, C., Carslaw, K. S., Coe, H., DeMott, P. J., Dunlea, E. J., Feingold, G., Ghan,  
1077 S., Guenther, A. B., Kahn, R., Kraucunas, I., Kreidenweis, S. M., Molina, M. J., Nenes, A., Penner, J.  
1078 E., Prather, K. A., Ramanathan, V., Ramaswamy, V., Rasch, P. J., Ravishankara, A. R., Rosenfeld, D.,  
1079 Stephens, G., and Wood, R.: Improving our fundamental understanding of the role of aerosol–cloud  
1080 interactions in the climate system, *Proceedings of the National Academy of Sciences*, 113, 5781–5790,  
1081 <https://doi.org/10.1073/pnas.1514043113>, 2016.
- 1082 Sorooshian, A., Anderson, B., Bauer, S. E., Braun, R. A., Cairns, B., Crosbie, E., Dadashazar, H., Diskin,  
1083 G., Ferrare, R., Flagan, R. C., Hair, J., Hostetler, C., Jonsson, H. H., Kleb, M. M., Liu, H., MacDonald,  
1084 A. B., McComiskey, A., Moore, R., Painemal, D., Russell, L. M., Seinfeld, J. H., Shook, M., Smith, W.  
1085 L., Thornhill, K., Tselioudis, G., Wang, H., Zeng, X., Zhang, B., Ziemba, L., and Zuidema, P.: Aerosol–  
1086 Cloud–Meteorology Interaction Airborne Field Investigations: Using Lessons Learned from the U.S.  
1087 West Coast in the Design of ACTIVATE off the U.S. East Coast, <https://doi.org/10.1175/BAMS-D-18-0100.1>, 2019.
- 1089 Stier, P., Van Den Heever, S. C., Christensen, M. W., Gryspeerdt, E., Dagan, G., Saleeby, S. M.,  
1090 Bollasina, M., Donner, L., Emanuel, K., Ekman, A. M. L., Feingold, G., Field, P., Forster, P., Haywood,  
1091 J., Kahn, R., Koren, I., Kummerow, C., L’Ecuyer, T., Lohmann, U., Ming, Y., Myhre, G., Quaas, J.,  
1092 Rosenfeld, D., Samset, B., Seifert, A., Stephens, G., and Tao, W.-K.: Multifaceted aerosol effects on  
1093 precipitation, *Nat. Geosci.*, 17, 719–732, <https://doi.org/10.1038/s41561-024-01482-6>, 2024.
- 1094 Su, W., Loeb, N. G., Xu, K.-M., Schuster, G. L., and Eitzen, Z. A.: An estimate of aerosol indirect effect  
1095 from satellite measurements with concurrent meteorological analysis, *Journal of Geophysical Research:*  
1096 *Atmospheres*, 115, <https://doi.org/10.1029/2010JD013948>, 2010.
- 1097 [Su, Y., Han, Y., Luo, H., Zhang, Y., Shao, S., Xie, X., Su, Y., Han, Y., Luo, H., Zhang, Y., Shao, S., and](https://doi.org/10.3390/rs14102453)  
1098 [Xie, X.: Physical-Optical Properties of Marine Aerosols over the South China Sea: Shipboard](https://doi.org/10.3390/rs14102453)  
1099 [Measurements and MERRA-2 Reanalysis. \*Remote Sensing\*, 14, <https://doi.org/10.3390/rs14102453>,](https://doi.org/10.3390/rs14102453)  
1100 [2022.](https://doi.org/10.3390/rs14102453)
- 1101 Sun, Q., Liang, B., Cai, M., Zhang, Y., Ou, H., Ni, X., Sun, X., Han, B., Deng, X., Zhou, S., and Zhao,  
1102 J.: Cruise observation of the marine atmosphere and ship emissions in South China Sea: Aerosol  
1103 composition, sources, and the aging process, *Environmental Pollution*, 316, 120539,  
1104 <https://doi.org/10.1016/j.envpol.2022.120539>, 2023.
- 1105 Tan, J., Huffman, G. J., Bolvin, D. T., and Nelkin, E. J.: Diurnal Cycle of IMERG V06 Precipitation,  
1106 *Geophysical Research Letters*, 46, 13584–13592, <https://doi.org/10.1029/2019GL085395>, 2019a.
- 1107 Tan, J., Huffman, G. J., Bolvin, D. T., and Nelkin, E. J.: IMERG V06: Changes to the Morphing  
1108 Algorithm, <https://doi.org/10.1175/JTECH-D-19-0114.1>, 2019b.

- 1109 Tu, Q., Zhao, Y., Guo, J., Cheng, C., Shi, L., Yan, Y., and Hao, Z.: Spatial and Temporal Variations of  
 1110 Aerosol Optical Thickness over the China Seas from Himawari-8, *Remote Sensing*, 13, 5082,  
 1111 <https://doi.org/10.3390/rs13245082>, 2021.
- 1112 Twomey, S.: Pollution and the planetary albedo, *Atmospheric Environment* (1967), 8, 1251–1256,  
 1113 [https://doi.org/10.1016/0004-6981\(74\)90004-3](https://doi.org/10.1016/0004-6981(74)90004-3), 1974.
- 1114 Twomey, S.: *The Influence of Pollution on the Shortwave Albedo of Clouds*, 1977.
- 1115 Wall, C. J., Norris, J. R., Possner, A., McCoy, D. T., McCoy, I. L., and Lutsko, N. J.: Assessing effective  
 1116 radiative forcing from aerosol–cloud interactions over the global ocean, *Proceedings of the National*  
 1117 *Academy of Sciences*, 119, e2210481119, <https://doi.org/10.1073/pnas.2210481119>, 2022.
- 1118 Wall, C. J., Storelvmo, T., and Possner, A.: Global observations of aerosol indirect effects from marine  
 1119 liquid clouds, *Atmospheric Chemistry and Physics*, 23, 13125–13141, [https://doi.org/10.5194/acp-23-](https://doi.org/10.5194/acp-23-13125-2023)  
 1120 [13125-2023](https://doi.org/10.5194/acp-23-13125-2023), 2023.
- 1121 Wang, B., LinHo, Zhang, Y., and Lu, M.-M.: Definition of South China Sea Monsoon Onset and  
 1122 Commencement of the East Asia Summer Monsoon, <https://doi.org/10.1175/2932.1>, 2004.
- 1123 Wang, B., Huang, F., Wu, Z., Yang, J., Fu, X., and Kikuchi, K.: Multi-scale climate variability of the  
 1124 South China Sea monsoon: A review, *Dynamics of Atmospheres and Oceans*, 47, 15–37,  
 1125 <https://doi.org/10.1016/j.dynatmoce.2008.09.004>, 2009.
- 1126 Wang, F., Guo, J., Wu, Y., Zhang, X., Deng, M., Li, X., Zhang, J., and Zhao, J.: Satellite observed  
 1127 aerosol-induced variability in warm cloud properties under different meteorological conditions over  
 1128 eastern China, *Atmospheric Environment*, 84, 122–132,  
 1129 <https://doi.org/10.1016/j.atmosenv.2013.11.018>, 2014.
- 1130 Wang, J.-J., Li, X., and Carey, L. D.: Evolution, Structure, Cloud Microphysical, and Surface Rainfall  
 1131 Processes of Monsoon Convection during the South China Sea Monsoon Experiment, *Journal of the*  
 1132 *Atmospheric Sciences*, 64, 360–380, <https://doi.org/10.1175/JAS3852.1>, 2007.
- 1133 Wang K.-Y., Sui C.-H., Lu M.-M., and Hong J.-S.: Cold Surge Impacts on the Structure, Energy Budget,  
 1134 and Turbulence of the South China Sea Boundary Layer, <https://doi.org/10.1175/MWR-D-23-0238.1>,  
 1135 2024a.
- 1136 Wang, S., Wang, Q., and Feingold, G.: Turbulence, Condensation, and Liquid Water Transport in  
 1137 Numerically Simulated Nonprecipitating Stratocumulus Clouds, 2003.
- 1138 Wang, Y., Zhao, P., Xiao, H., and Zhang, P.: Aerosol effects on liquid cloud microphysical properties in  
 1139 south China: Land–ocean contrasts, *Atmospheric Pollution Research*, 15, 102032,  
 1140 <https://doi.org/10.1016/j.apr.2023.102032>, 2024b.
- 1141 Wang, Y., Li, J., Fang, F., Zhang, P., He, J., Pöhlker, M. L., Henning, S., Tang, C., Jia, H., Wang, Y.,  
 1142 Jian, B., Shi, J., and Huang, J.: In-situ observations reveal weak hygroscopicity in the Southern Tibetan

- 1143 Plateau: implications for aerosol activation and indirect effects, *npj Clim Atmos Sci*, 7, 77,  
1144 <https://doi.org/10.1038/s41612-024-00629-x>, 2024c.
- 1145 Wang, Y., Jia, H., Zhang, P., Fang, F., Li, J., Zhu, L., Wang, Y., Wang, T., and Li, J.: Sensitivity of cloud  
1146 microphysics to aerosol is highly associated with cloud water content: Implications for indirect radiative  
1147 forcing, *Atmospheric Research*, 309, 107552, <https://doi.org/10.1016/j.atmosres.2024.107552>, 2024d.
- 1148 Watters, D. and Battaglia, A.: The Summertime Diurnal Cycle of Precipitation Derived from IMERG,  
1149 *Remote Sensing*, 11, 1781, <https://doi.org/10.3390/rs11151781>, 2019.
- 1150 Watters, D., Battaglia, A., and Allan, R. P.: The Diurnal Cycle of Precipitation according to Multiple  
1151 Decades of Global Satellite Observations, Three CMIP6 Models, and the ECMWF Reanalysis, *Journal*  
1152 *of Climate*, 34, 5063–5080, <https://doi.org/10.1175/JCLI-D-20-0966.1>, 2021.
- 1153 Wu, Z., Jiang, C., Conde, M., Chen, J., and Deng, B.: The long-term spatiotemporal variability of sea  
1154 surface temperature in the northwest Pacific and China offshore, *Ocean Science*, 16, 83–97,  
1155 <https://doi.org/10.5194/os-16-83-2020>, 2020.
- 1156 Xiao, H.-W., Xiao, H.-Y., Luo, L., Shen, C.-Y., Long, A.-M., Chen, L., Long, Z.-H., and Li, D.-N.:  
1157 Atmospheric aerosol compositions over the South China Sea: temporal variability and source  
1158 apportionment, *Atmospheric Chemistry and Physics*, 17, 3199–3214, [https://doi.org/10.5194/acp-17-](https://doi.org/10.5194/acp-17-3199-2017)  
1159 [3199-2017](https://doi.org/10.5194/acp-17-3199-2017), 2017.
- 1160 Yost, C. R., Minnis, P., Sun-Mack, S., Chen, Y., and Smith, W. L.: CERES MODIS Cloud Product  
1161 Retrievals for Edition 4—Part II: Comparisons to CloudSat and CALIPSO, *IEEE Transactions on*  
1162 *Geoscience and Remote Sensing*, 59, 3695–3724, <https://doi.org/10.1109/TGRS.2020.3015155>, 2021.
- 1163 Yuan, C.-S., Chuang, H.-L., Tseng, Y.-L., Li, T.-C., Soong, K.-Y., and Cheng, W.-H.: Long-range  
1164 transport and source apportionment of marine fine particles in the Taiwan Strait and South China Sea  
1165 Intersection: Spatiotemporal variations and chemical fingerprints, *Atmospheric Environment*, 339,  
1166 120867, <https://doi.org/10.1016/j.atmosenv.2024.120867>, 2024.
- 1167 Yuan, T., Li, Z., Zhang, R., and Fan, J.: Increase of cloud droplet size with aerosol optical depth: An  
1168 observation and modeling study, *Journal of Geophysical Research: Atmospheres*, 113,  
1169 <https://doi.org/10.1029/2007JD008632>, 2008.
- 1170 Zhang, C., Xu, H., Li, Z., Xie, Y., and Li, D.: Maritime Aerosol Optical and Microphysical Properties in  
1171 the South China Sea Under Multi-source Influence, *Sci Rep*, 9, 17796, [https://doi.org/10.1038/s41598-](https://doi.org/10.1038/s41598-019-54483-6)  
1172 [019-54483-6](https://doi.org/10.1038/s41598-019-54483-6), 2019.
- 1173 Zhang, G. J., Ramanathan, V., and McPhaden, M. J.: Convection-Evaporation Feedback in the Equatorial  
1174 Pacific, 1995.

1175 Zhang, Y. and Wang, K.: The Changing Morphology of Global Precipitation Systems during the Last  
1176 Two Decades, *Bulletin of the American Meteorological Society*, 105, E1861–E1880,  
1177 <https://doi.org/10.1175/BAMS-D-23-0106.1>, 2024.

1178 Zhao, C., Sun, Y., Yang, J., Li, J., Zhou, Y., Yang, Y., Fan, H., and Zhao, X.: Observational evidence  
1179 and mechanisms of aerosol effects on precipitation, *Science Bulletin*, 69, 1569–1580,  
1180 <https://doi.org/10.1016/j.scib.2024.03.014>, 2024.

1181 Zheng, B., Qu, J., Huang, Y., Peng, D., Gu, D., Li, C., and Huang, R.: Evaluating the Seasonal Cycle of  
1182 the South China Sea Monsoon in CMIP6 Models, *J Meteorol Res*, 39, 322–337,  
1183 <https://doi.org/10.1007/s13351-025-4170-x>, 2025.

1184 Zheng, H., Liu, M., Lohmann, R., Li, D., Vojta, S., Katz, S., Wang, W., Ke, H., Wang, C., and Cai, M.:  
1185 Gaseous polycyclic aromatic hydrocarbons over the South China Sea: Implications for atmospheric  
1186 transport under monsoon influences, *Marine Pollution Bulletin*, 191, 114982,  
1187 <https://doi.org/10.1016/j.marpolbul.2023.114982>, 2023.

1188 Zheng, X., Xi, B., Dong, X., Wu, P., Logan, T., and Wang, Y.: Environmental effects on aerosol–cloud  
1189 interaction in non-precipitating marine boundary layer (MBL) clouds over the eastern North Atlantic,  
1190 *Atmos. Chem. Phys.*, 22, 335–354, <https://doi.org/10.5194/acp-22-335-2022>, 2022.

1191 Zhu, S., Xiao, Z., Che, H., and Chen, Q.: Impact of aerosols on warm clouds over the Sichuan Basin,  
1192 China in winter based on the MERRA-2 reanalysis dataset, *Atmospheric Pollution Research*, 13, 101342,  
1193 <https://doi.org/10.1016/j.apr.2022.101342>, 2022.

1194 Zhu, S., Li, Z., Chen, M., Wen, Y., Gao, S., Zhang, J., Wang, J., Nan, Y., Ferraro, S. C., Tsoodle, T. E.,  
1195 and Hong, Y.: How has the latest IMERG V07 improved the precipitation estimates and hydrologic  
1196 utility over CONUS against IMERG V06?, *Journal of Hydrology*, 645, 132257,  
1197 <https://doi.org/10.1016/j.jhydrol.2024.132257>, 2024.

1198